coatings

MDPI

Review

Inclusions and Segregations in the Selective Laser-Melted Alloys: A Review

Mahdi Yeganeh *, **Zahra Shahryari**, **Ali Talib Khanjar**, **Zeinab Hajizadeh** and **Fatemeh Shabani**

Department of Materials Science and Engineering, Faculty of Engineering, Shahid Chamran University of Ahvaz, Ahvaz 61357-83151, Iran; zahra2005shahryari@yahoo.com (Z.S.); yeganehmahdi@yahoo.com (A.T.K.); zeinabhahizadeh@gmail.com (Z.H.); shabani.metal85@gmail.com (F.S.)
* Correspondence: m.yeganeh@scu.ac.ir

Abstract: This paper aims to review some important microstructural defects arising in the alloys manufactured by selective laser melting (SLM) or laser powder bed fusion (LPBF). During the manufacturing process, various defects can occur in metals, which can negatively impact their mechanical properties and structural integrities. These defects include gas pores, lack of fusions, keyholes, melt pools, cracks, inclusions, and segregations. In this review, heterogeneities such as inclusion and segregation defects are discussed. Other types of defects have been comprehensively discussed in other reviews. Inclusions refer to foreign ceramic particles that are present within the metal, whereas segregations refer to the uneven distribution of alloying elements within the microstructure of the metal. The cause of appearance, effect of different parameters, and methods to reduce them in the final part are also reviewed. The effects of these defects on the integrity of the produced parts are discussed. Solutions for the elimination or minimization of these defects are also suggested. Post treatments and modifications of an alloy's composition can also help to improve its material properties and reduce its defect concentration.

Keywords: selective laser melting (SLM); laser powder bed fusion (LPBF); inclusions; segregations

Citation: Yeganeh, M.; Shahryari, Z.; Talib Khanjar, A.; Hajizadeh, Z.; Shabani, F. Inclusions and Segregations in the Selective Laser-Melted Alloys: A Review. *Coatings* **2023**, *13*, 1295. https://doi.org/10.3390/coatings13071295

Academic Editor: Gilda Renna

Received: 23 June 2023
Revised: 19 July 2023
Accepted: 21 July 2023
Published: 24 July 2023

1. An Introduction to Additive Manufacturing

The method of leveraging 3D model data to produce complicated geometries and structures is known as additive manufacturing (AM). Another name for it is solid–freeform fabrication, rapid prototyping, and layer manufacturing. As compared to traditional subtractive manufacturing processes dependent on powder or wire feedstock heated or fused through a high temperature reservoir and created using an electronically controlled heat source mechanism, this method involves layer-by-layer production. The time between idea conception and new product creation can be shortened by adopting this technique. Early in the 1980s, Charles Hull was the one who first commercialized this technique. Currently, AM is utilized to make parts for rocket engines, artificial heart pumps, corneas, implants, bridges, jewelry, food products, vehicle parts, and residences. By adding material layer by layer using a 3D printer, the additive manufacturing process creates 3D elements from CAD data [1,2]. An overview of important facets of the AM approach was given in the roadmap Bourell et al. released in 2009, comprising [3]:

- Modeling and management of processes;
- Resources, procedures, and equipment;
- Uses in biomedicine;
- Uses for sustainability and energy.

According to recent research, additive manufacturing can significantly reduce the need for machine tools in traditional casting techniques, which has an effect on the production process [4]. A number of charming features make AM appealing, including lightweight design, automation, greater flexibility, no material waste, reduced cost, no need for skilled craftspeople due to an automated process, very little noise, and eco-friendliness. However, there are several disadvantages to adopting AM technology, such as the expensive machine, restrictions on object size, higher unemployment, sluggish construction pace, and more. However, contemporary R&D has reduced the price of 3D printing devices, making them more affordable and available in classrooms, labs, libraries, homes, etc. [1].

Today, both metallic and non-metallic materials can be printed in a huge variety [5,6]. Nowadays, porcelain, wax, metals, concrete, conductive polymers, acrylonitrile butadiene styrene (ABS), adhesive-coated strips, and polylactic acid (PLA) may all be produced by utilizing additive manufacturing (AM) technology [1].

2. Classification of AM

According to the guidelines set by the ASTM-F42 committee, additive manufacturing (AM) can be classified into seven categories. One common classification system is based on these guidelines, which include vat photopolymerization (VP), material jetting (MJ), binder jetting (BJ), material extrusion (ME), sheet lamination (SL), powder bed fusion (PBF), and directed energy deposition (DED) [7]. Figure 1 shows different AM methods [8]. AM technology allows for the production of components using a wide range of materials, each with its unique properties and applications. As technology continues to evolve, we can expect to see the development of new and improved materials that will further expand the capabilities of AM in various industries.

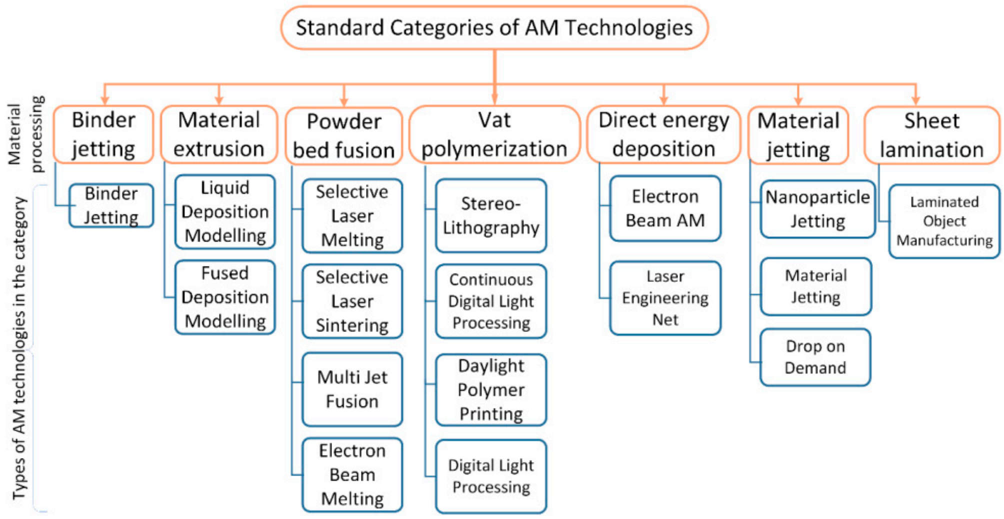

Figure 1. Different types of additive manufacturing [8].

3. Materials

Any production method, including AM processes, requires that the material be prepared in a manner that is appropriate with the technique (for example, powder, sheet, wire, or liquid). For instance, the feedstock for photopolymer jetting and vat polymerization must be a thermoplastic polymer or plastic monomer that can crosslink when subjected to external magnetic waves [9]. AM components can be manufactured from ceramics, polymers, metals, plastics, and their combinations. There is still room for improvement in the materials. Metals are widely used in AM due to their excellent mechanical and thermal properties. Additive manufacturing techniques such as powder bed fusion and directed energy deposition have been used to produce high-strength metal components such as aerospace parts, automotive components, and medical implants. Polymers are another popular material used in AM, mainly due to their low cost, light weight, and ease of processing. AM techniques such as fused deposition modeling and stereolithography have been used to produce polymer components with high accuracy and precision, making them suitable for prototyping and low-volume production. Ceramics are also commonly used in AM, particularly for applications that require high strength, wear resistance, and high-temperature stability. AM techniques such as powder bed fusion and stereolithography have been used to produce ceramic components such as biomedical implants, aerospace components, and electronic devices. Composites are a relatively new class of materials that have gained popularity in AM due to their unique combination of properties. Composites are made by combining two or more materials with different properties to create a material with improved strength, stiffness, and durability. AM techniques such as fused filament fabrication and binder jetting have been used to produce composite components such as automotive parts, aerospace components, and sporting equipment [1,4,7,10,11].

4. Laser Powder Bed Fusion (LPBF)/Selective Laser Melting (SLM)

In additive fabrication, the most common type is powder bed fusion. Thin films of powder are put to a prepared surface during powder bed fusion, and energy is delivered at specified locations on the model to fuse the powder [12]. A 3D part is created by applying successive layers of powder and then repeating the process until the part is complete. Powder bed fusion is alternatively designated selective laser melting (SLM), selective laser sintering (SLS), direct metal laser melting, and electron beam melting (EBM). A powder bed fusion machine melts instead of sinters parts with full densities [12,13].

In LPBF/SLM, several steps are involved, from preparing CAD data to withdrawing fabricated parts from the building plate. Before uploading CAD data to SLM machines for component manufacturing, STereoLithography (STL) files must be processed by software. This process enables laser scanning of individual layers and supports dangling features. Inside a building chamber, a small film of metal powder is applied to the substrate plate to begin the building process. Based on the collected data, the powder is applied, heated, and fused using a high-energy density laser. Following the laser scanning, a new powder layer is placed, and that layer is again examined. Every layer of powder must be added in order to construct the pieces, and then the process will continue. Modification of the parameters such as laser power, scanning speed, hatch spacing, and layer thickness can lead to the fusion a single melt vector completely with the surrounding melt vectors. A separate component can be manually or electrically discharged (EDM) separated from the substrate plate after laser scanning has been completed. All steps of the process are automated, except for preparing the data and removing fabricated components from the platform [13–15]. Figure 2 illustrates the concept of LPBF building [14].

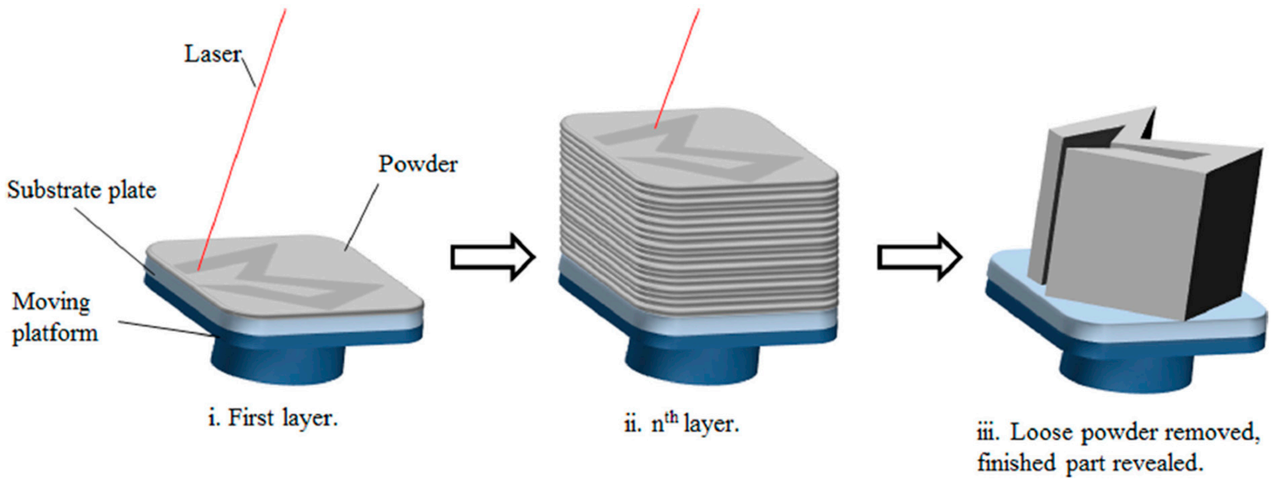

Figure 2. Scheme of LPBF process: (**i**) Laser melts specific areas of the powder bed (**ii**), Repeating the process for following layers, and (**iii**) Removing unattached powder and revealing the finished product "Reprinted with permission from Ref. [14] 2015. AIP Publishing".

Often, an inert atmosphere is provided by nitrogen or argon gas in the building chamber for protection against oxidation during the LPBF process. In addition, some LPBF machines are able to pre-heat either the build chamber or the substrate plate. Between 20 to

100 μm is the typical thickness of the layer [14,16]. It has been demonstrated that LPBF can fully melt powder materials, producing near-net-shape parts without post-processing. An LPBF process is more efficient, faster, and reliable than binder-based laser sintering methods [12–14]. Nevertheless, this laser method can result in various defects in the final parts, which may affect the alloy's performance. As a result, the strength and durability of the alloys may be compromised. This can lead to inferior performance and reduced reliability of the parts. Therefore, it is necessary to investigate and study the emerging defects in the SLM-manufactured alloys.

Microstructure of SLM Parts

In Figure 3, a schematic representation depicts the dependence of grain size and shape on solidification conditions. Increasing energy density leads to a reduction in temperature gradient. An equiaxed grain shape forms under a high solidification velocity and low temperature gradient, whereas a planar grain structure forms under high temperature gradient and low solidification velocity. A columnar grain shape is formed in the intermediate region (grey area in Figure 3). When transitioning to AM conditions, a cellular dislocation structure also forms due to a higher solidification velocity and larger temperature gradient. The SLM parameters fall within the columnar region, but adjustments to the parameters can result in an equiaxed grain structure for the isotropic material properties. Increasing both solidification velocity and temperature gradient brings the conditions closer to the SLM process, whereas decreasing the velocity and gradient leads to conditions similar to conventional casting [17].

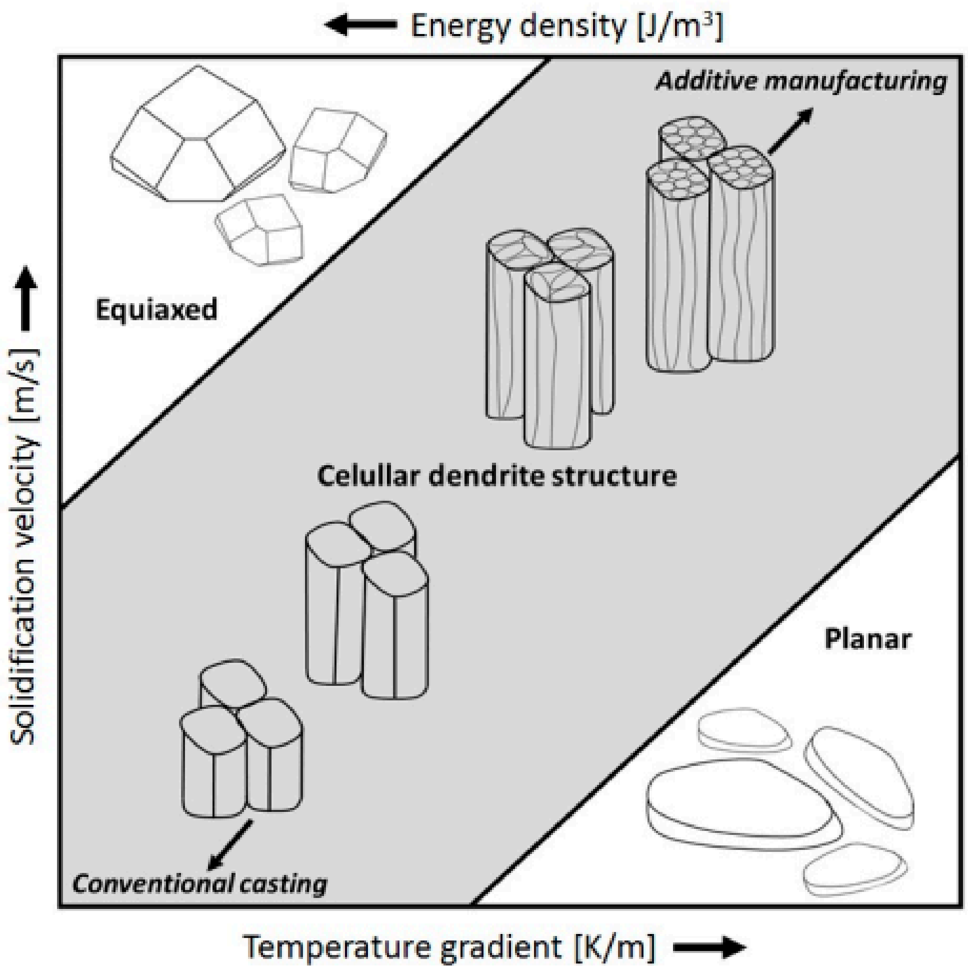

Figure 3. A schematic diagram illustrating the influence of solidification velocity and temperature gradient on the microstructure [17].

5. SLM and the Defects

Despite the fact that the SLM techniques have a significant benefit in that they can produce intricate parts with a significant material utilization rate, the process is, nevertheless, prone to flaws, including porosities, unfilled fusion holes, cracks, and impurities because of the aforementioned causes. Due to the risk these flaws provide to the mechanical and physical characteristics of manufactured parts, their usage in SLM is limited [18]. Typical morphological defects in alloys manufactured by SLM techniques are presented in this paper, including porosities, cracks, keyholes, inclusions, segregations, incomplete fusion holes, surface roughness, and balling defects. Figure 4 shows defects in SLM components. Numerous of these flaws may adversely affect the SLM alloys' mechanical, chemical, and physical characteristics. Remaining stress and anisotropy, which can affect the alloy in two different ways, are two more issues with the SLM process. Relative stress, for example, may increase the corrosion resistant property of stainless steel alloys created using SLM [19–21]. Several studies have found that fine inclusions do not degrade the corrosion resistances of alloys [22,23]. Researchers discovered that SLM alloy microstructures showed reduced segregation than conventional ones, improving the mechanical and electrochemical characteristics of AM alloys [24]. Biomedical implant materials must contain pores in order to develop bone tissue. Additionally, the morphological properties of pores, including porosity, pore size, and pore interconnection, play a key role in bone regeneration [25,26]. An alloy's performance can be adversely affected by some morphological defects. On the other hand, some defects can trigger the formation the others. According to the literature, Al7050 solidification cracks are caused by Cu segregation at the boundaries of dendrites [27], or Mo shows some cracks when residual stress surpasses the fracture strength [28]. Moreover, it was reported that some defects such as LOF are observed in the melt pool boundaries [29], or melt pool fluctuations can lead to the formation of LOF defects [30]. In addition, some defects, including cracks, roughness, porosities, etc., can be reduced or be optimized during the SLM process, whereas some other defects such as melt pool boundaries or inclusions are the intrinsic features in the SLM parts, which should be considered in the desired applications. Some parameters can reduce a specific defect, whereas the others reduce another defects. For example, pore formation is mainly influenced by laser power and hatch space, according to Vilanova et al. [31]. While most reviews have primarily focused on porosities and cracks, it is important to note that other significant imperfections also exist, such as inclusions and segregations. These defects can have a substantial impact on the mechanical properties of the material and must be addressed during the manufacturing process to ensure optimal quality and reliability. In this paper, inclusions and segregation defects will be reviewed and discussed.

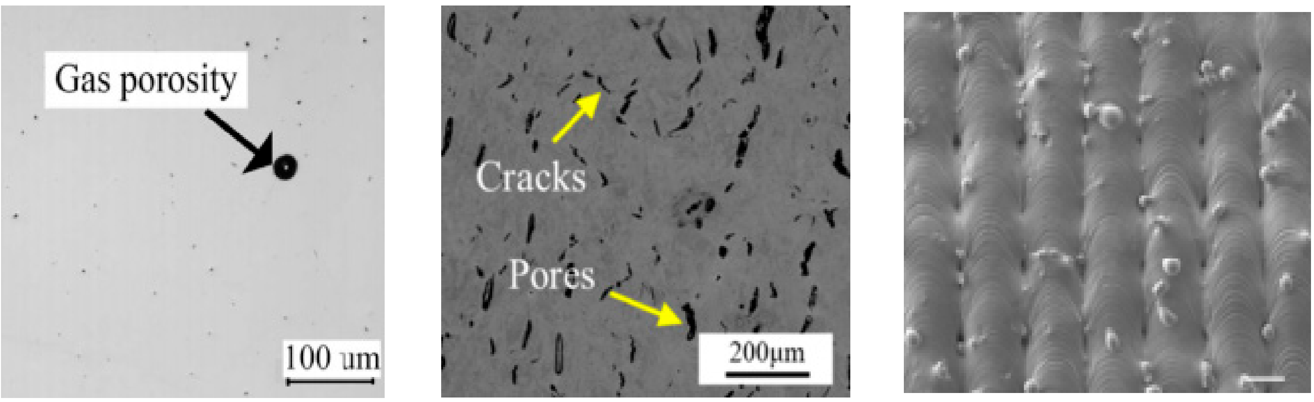

(**a**) (**b**) (**c**)

Figure 4. *Cont.*

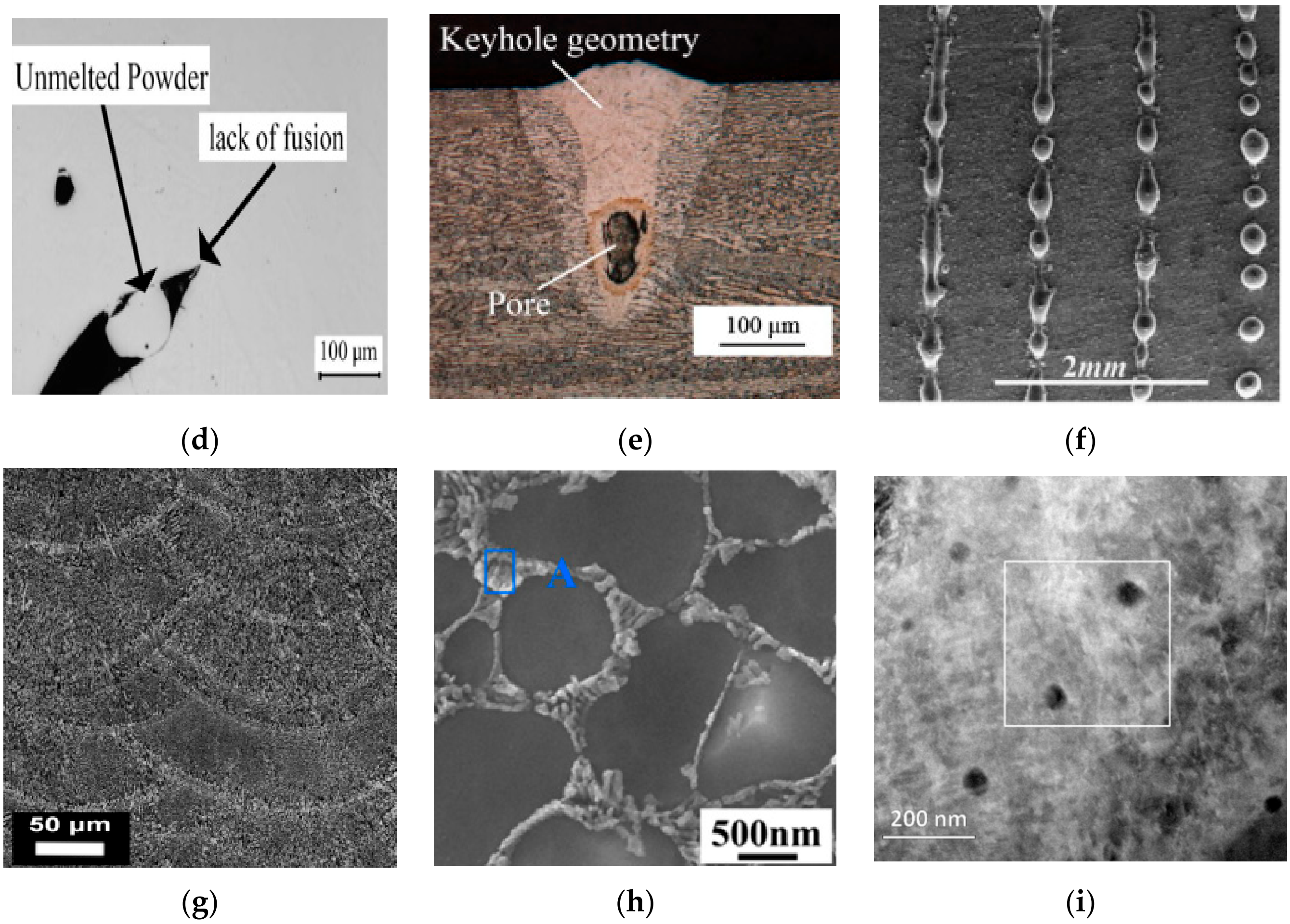

Figure 4. Some important defects in the SLM- manufactured alloys. (**a**) Gas pores [32], (**b**) Crack [33], (**c**) Roughness [34], (**d**) LOF [35], (**e**) Keyhole [32], (**f**) Balling [32], (**g**) Melt pool [36], (**h**) Segregation [37], (**i**) Inclusion [38].

5.1. Inclusions

Due to rapid cooling conditions and the availability of trace oxygen elements in the containers of SLM instruments, inclusions (oxide/non-oxide) appear mostly in the nano- to micro-meter size range during the AM process [5,23,39–41]. Additionally, during the operation, impurities in the feedstock powder can aggregate and stay intact during the post-treatments [42–44]. One of the main alloy groups that tend to show inclusions are stainless steels. Conventionally processed/post-processed stainless steel is known to contain a different precipitates, including oxides of transition metals (Fe, Cr, Ni, Mn, Mo), (Al–Mg–Si–Ca)-oxide, and silicon, and non-oxides, including transition-metal carbides, sulfides, phosphides, and intermetallic phases [45–51]. Additionally, compared to other transition metal (Fe, Cr, Ni, and Mo) oxides, the oxidation of Mn and Si inclusions in the AM alloy resulted in the largest reduction in the Gibbs free energy, which promoted the production of Mn-Si-O compared to other oxide precipitates [45].

Figure 5 shows the TEM micrograph taken from an SLM-produced part prepared under a chamber with an oxygen content of 0.1%. In addition to austenite grains visible from their orientation contrast, spherical inclusions are also visible. Nano-sized inclusions with average diameters of 50 nm are well dispersed inside the steel matrix. Inclusions in spherical shapes are amorphous, whereas neighboring sites are crystalline. Amorphous oxide nano-inclusions formed in situ contain Si, O, and a small amount of Cr. Tensile and yield strengths of 316L stainless steel at room temperature were 703 and 456 MPa, respectively. These values are higher than those of 316L steel that was traditionally cast. 316L steel exhibited high ductility with 46% elongation due to multi-scale dimples, extremely fine oxide nano-inclusions, and was well-distributed in the steel matrix contamination [52].

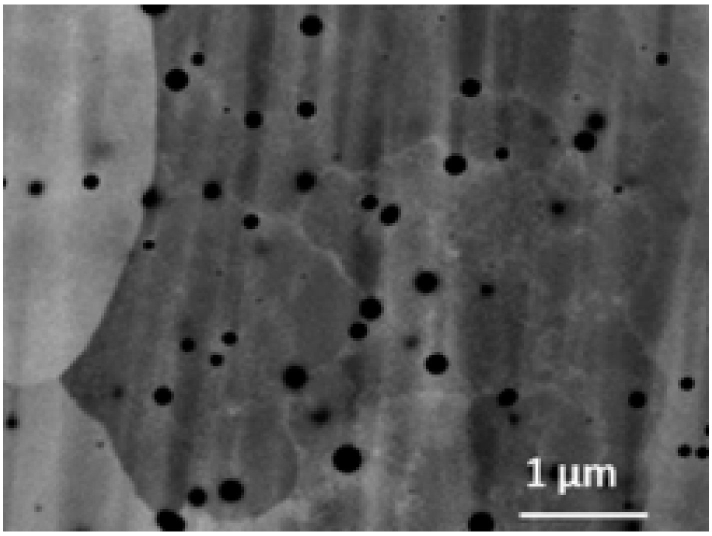

Figure 5. HRTEM micrograph taken from nano-inclusions with darker resolution "Reprinted with Permission from Ref. [52], 2015, Royal Society of Chemistry".

Moreover, in the SLM process, the formation of some typical inclusions like MnS can be reduced due to rapid cooling [43,53,54]. The inclusion of MnS cannot be seen because of rapid solidification rates (usually 10^7 K/s). In contrast, there were 0.1 to 10 s for the nucleation and diffusional growth of MnS precipitates in the wrought, compared to a solidification rate of 273 to 373 K/s in a traditional casted alloy [55,56]. During gas atomization, the powder feedstock is rapidly cooled, resulting in amorphous inclusions that contain manganese, chromium, silicon, and oxygen surrounded by small crystalline MnS particles. Amorphous regions surrounded the exterior of the inclusions created by additive manufacturing include rhodonite ($MnSiO_3$) and spinel ($MnCr_2O_4$) [43].

As-deposited and post-processed stainless steels manufactured using AM processes can develop oxide inclusions due to high oxygen levels in the powder [5,6,41,57–60]. Stainless steels' microstructural developments, mechanical characteristics, and corrosion resistances have all been known to be impacted by these inclusions [43]. It was discovered that the inclusions in the SLM alloys are entirely distinct from those in the conventional alloys in terms of both shapes and contents, as previously stated. Figure 6a,b, respectively, demonstrates the usual inclusions in the Roll and SLM specimens [58]. In a roll specimen, there is a Ti-based, sharp-edged inclusion that may include TiN and TiC phases. It has been established that the presence of TiN significantly affects stainless steel's ability to resist corrosion [61,62]. Additionally, the emergence of Ti-based inclusions and the drop in Cr concentration both have the potential to hasten the creation of galvanic pairs among the inclusions and matrix, which would result in corrosion [57,61]. In contrast, a spherical oxide inclusion in the SLM sample is more abundant in Cr, Mn, and Si. As a consequence, combinations of SiO_2, Cr_2O_3, Fe_2O_3, and MnO_2 are likely the most common oxides [58]. Local galvanic cells are also less likely to develop inside or close to inclusions because there are not any noticeable variations in the Cr content.

Additionally, Figure 7a,b shows the morphology and EDS findings of the 17-4 PH stainless steel specimen, illuminating the second phases found in the alloy matrix [5]. Elongated-ferrite stringers, seen in Figure 7a [63], are the second detected phase in the wrought specimen. As seen in Figure 7b, the majority of the second phase of the SLMed alloy is composed of SiO_2, MnO_2, Cr_2O_3, and Al_2O_3 [6]. AM's mixture of stainless steel was found to primarily contain amorphous silicates that contained Mn and Cr. Many compounds may deposit during the solidification stage of SLM process.

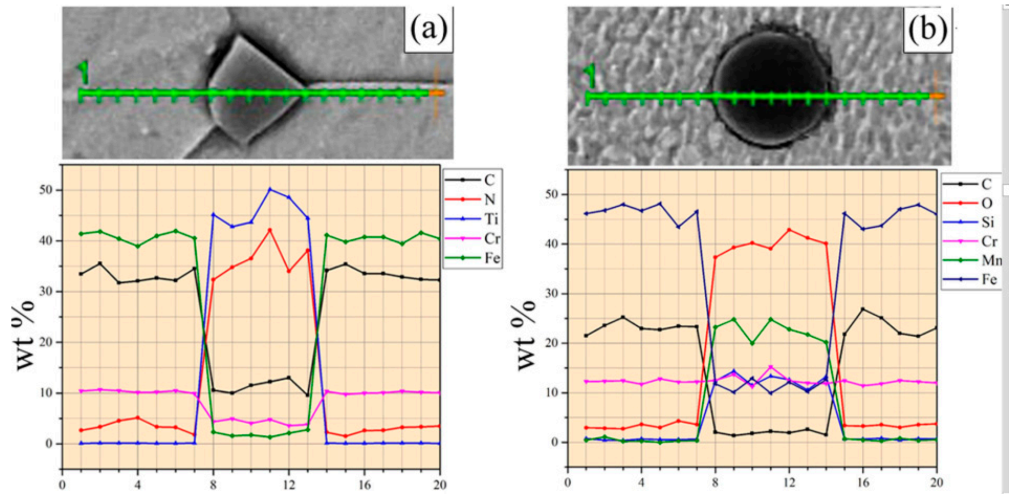

Figure 6. Line EDS and FESEM images pertaining to inclusion in the (**a**) Roll and (**b**) SLM sample, "Reprinted with Permission from Ref. [58], 2022, AIP Publishing".

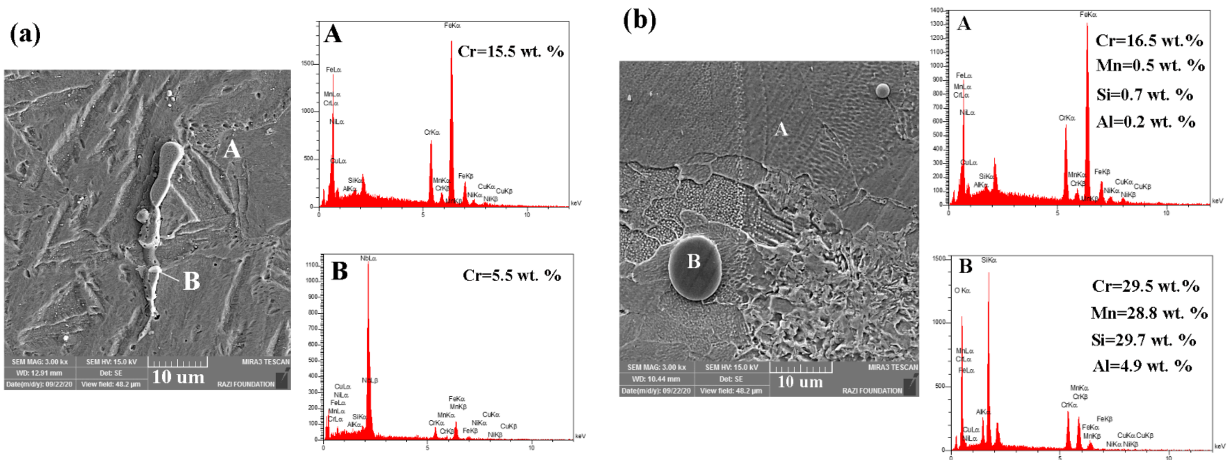

Figure 7. (**a**) ×3000 magnification FESEM images and (**b**) EDS data of wrought and SLMed 17-4 PH stainless steel: A: matrix, B: inclusion. Reprinted with Permission from [5], 2021, AIP Publishing.

The development of non-soluble spheres in high viscosity silicate melts through the use of a low inclination to iron can reduce surface tension [39]. Hsu and his colleagues also found that the as-built 17-4 PH stainless steel created by the SLM process contained Mn-Si rich micro oxide particles [64]. The quantity of the Cr decline in the wrought sample compared to the SLMed counterpart was larger, according to EDS data, from the matrix (A) through the second phase (B). The localized galvanic cell was more likely to occur in the wrought specimen due to the larger variances in Cr content. The B point in the wrought specimen would be in anodic condition relative to the A site after exposure to the corrosive fluids because of its substantially reduced Cr content. Yet, the SLMed sample's B point had a greater Cr concentration than the A site did. Also, it was demonstrated [65] that corrosion increased as the cathode/anode area ratio rose. Therefore, compared to its SLMed counterpart, a wrought specimen with a low anodic region may experience more serious corrosion problems [5].

However, some thermal treatments may cause MnS phases to form around inclusions. Due to insufficient time to separate MnS during the SLM process, the presence of Mn and S in the SLM alloy implied that MnS may have formed during heat treatment. Inclusions containing potentially dangerous elements like sulfur and the formation of local corrosion cells as a result of the dramatic reduction in chromium in the inclusions may have had the biggest effects on the corrosion performance of the heat-treated specimen at 1050 °C [57].

Additionally, heating should have no effect on the nucleation and propagation of M-S on oxide inclusions, which should only occur during solidification/cooling at temperatures more than 1273 K [45].

There needs to be more thorough research on the impact of inclusions on the function of SLMed components. On the other hand, the individual effect of lone particles in any alloy is not easy to investigate. According to some authors, inclusions can promote heterogeneous nucleation and grain refinement during solidification [66,67]. In addition, they can reduce galvanic effects in the corrosion application compared to conventional inclusions [5,6,58]. Furthermore, inclusions result in the material being stressed in the tensile process so that the actual stress is higher than the external force, resulting in the material breaking at a low-stress level, thereby reducing the strength of the wall parts [68]. As a result of grinding and polishing, most inclusions separate from the matrix, leaving "holes" in it, indicating that they are only weakly adhered to the matrix [69]. Coexistence of oxides (e.g., Al-rich oxide) and nitrides (e.g., TiN) has been reported frequently in recycled powders of Alloy 718. Due to their brittle nature and high strain localization, such inclusions have typically been demonstrated to be extremely harmful to mechanical characteristics [42]. It is more important to avoid agglomeration and clustering of inclusions during manufacturing [42]. Crack branching can also be promoted by inclusion dissolution in AM 316L stainless steel [70]. Some oxide inclusions established electrochemical potential differences between inclusions and metal matrixes, making the inclusion site more sensitive to corrosion. As a result, grain boundary strength can be weakened, and oxidation can be faster near the inclusions [46]. The presence of oxides acted as the starting point for the development of micro-voids and decreased toughness [70]. Enhanced cathodic activities are observed in additively manufactured magnesium alloys due to the presence of MgO inclusions [44]. SLM material may be imperfect due to the inclusion of small particles in the powder bed, resulting in laser absorption effects [71]. Briefly, the impact of inclusion on the performance of an alloy has a dual aspect. If its presence hinders the formation of harmful phases, including MnS, shows strong interface, and reduces the galvanic effect, it can be concluded that the formation of inclusion is useful. But, in many cases, the weak interfaces, agglomeration, crack initiators, and galvanic effect promotor can lead to a deterioration in the performance of parts. Figure 8 displays the fracture surface of the AM 316L SS specimen, indicating consistent complete fracture. The specimen produced a single fragment with signs of plastic deformation. High-resolution SEM revealed oxide inclusions in the dimples. This suggested that oxides acted as initiation sites for micro-void formation, leading to reduced toughness [70].

Some efforts have been made to provide fewer inclusions in the AM alloy by using Si- and Mn-free powders as oxygen getters. But, the results showed that Cr can replace this position and takes reactions with oxygen [72]. Also, the formation stabilities of inclusions can induce some inevitable compositions, and some thermodynamic studies revealed that their presences were predictable. It was reported that at the low oxygen composition in the wrought material, the spinel inclusion phase ($MnCr_2O_4$) forms at a temperature of 1434 °C for stainless steel, which is moderately lower than the solidus temperature. However, it is predicted that the similar spinel phase will form at a temperature of 1596 °C, which is around 250 °C higher than the solidus. It was shown that the amount of spinel phase generated increased almost two orders of magnitude with a rise in oxygen composition from 0.01 to 0.1 wt.%. The increase in oxygen content also increased the spinels' formation temperatures, which reached nearly 1800 °C at 0.1 wt.%. Due to the fact that these high formation temperatures were well within the liquid phase, it was determined that conventional solid-state heat treatment techniques could not eliminate the spinel phase [43]. In addition, some thermodynamic calculations showed the presence of oxides in the composition of a stainless steel alloy fabricated by the SLM technique [73]. Figure 9 illustrates that the FCC matrix phase remained stable until a temperature of 1410 °C was reached. $M_{23}C_6$, a metal carbide precipitate, formed at temperatures below 500 °C but dissolved at 1020 °C. Oxide phases were present throughout the temperature range, with Cr_2O_3

becoming stable at 950 °C and higher, $MnSiO_3$ favoring up to 970 °C, and SiO_2 remaining thermodynamically stable within 910–1220 °C [73].

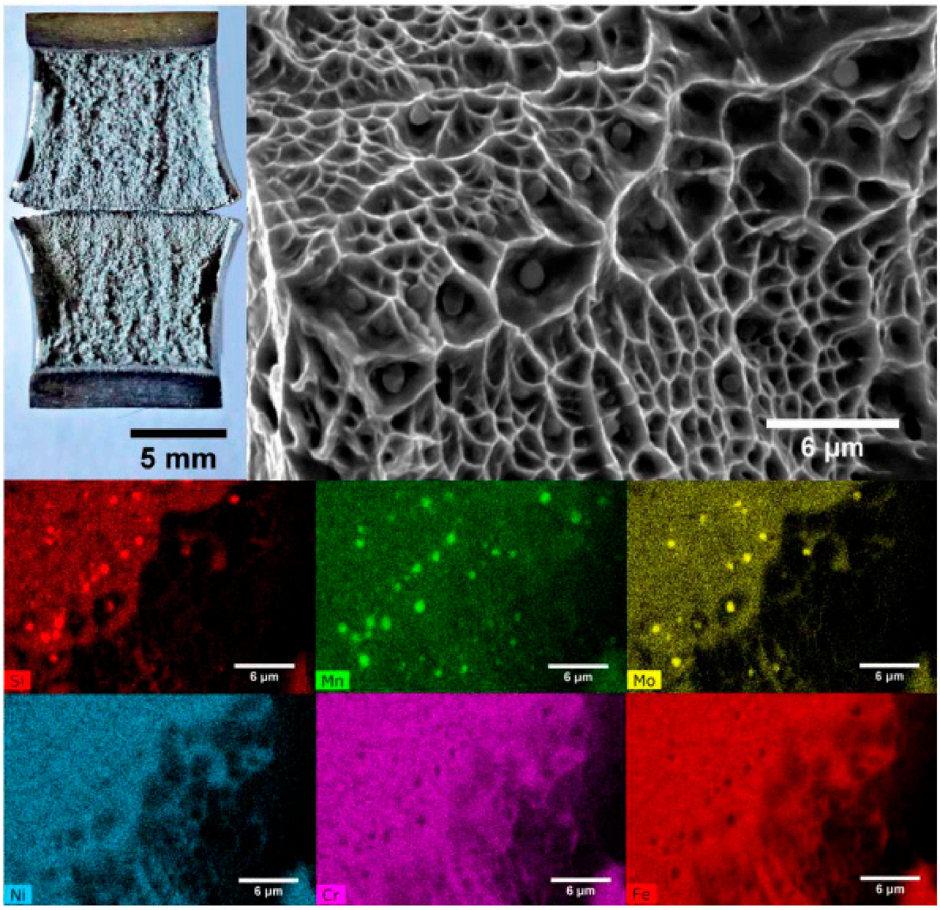

Figure 8. SEM and EDS of fractured 316L SS SLM manufactured alloy, "Reprinted with Permission from Ref. [70], 2018, Elsevier".

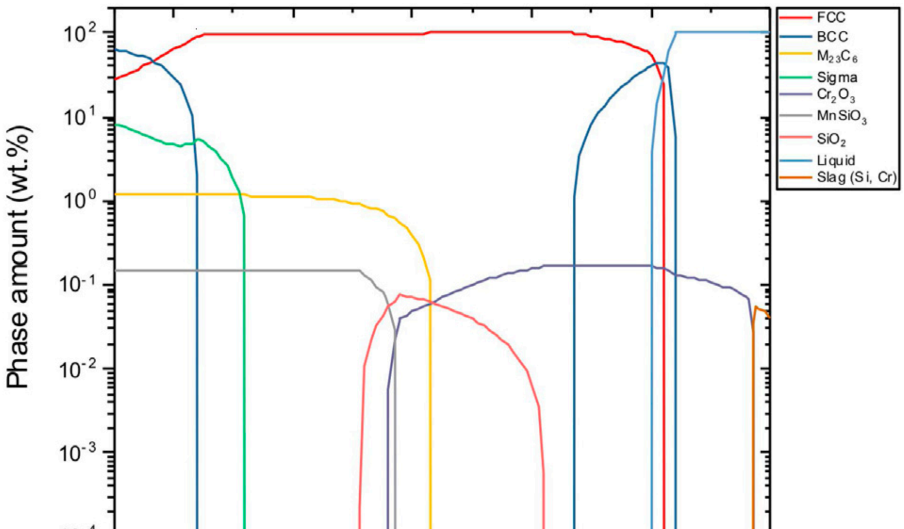

Figure 9. Thermodynamic calculations and examine the correlation between temperature and phase fraction in SLM-manufactured 316L SS [73].

5.2. Segregation/Micro-Segregation

Solute elements can segregate as a result of changes in their solubilities in both liquid and solid forms. The length scale over which this happens is determined by the kinetics of solidification, more precisely the degree of undercooling that is correlated with the system's cooling rate. As may be observed, the microstructure of the additively made material has a significantly finer cellular length scale than the morphology of conventional cast alloy material, which suggests that the additively manufactured material will cool more quickly [74]. Solute segregation is prominent in cellular and dendritic growth modes during the SLM process [75], but the range of segregation is very limited compared to the conventional alloys. In other words, segregation in the additive manufactured alloys can be denoted as micro-segregation. Element segregation is essential for predicting the solidification structure and mechanical characteristics of alloy components during additive manufacturing [76]. A key metric of material homogeneity is micro-segregation. This happens because the initial concentration of the solid is below the level at which the balance is reached. Higher concentrations of the solute, such as inter-dendritic regions and grain borders, are produced when the surplus solute is partitioned into the liquid [77].

According to some experts, segregation may be avoided by a rapid cooling rate before and after the SLM process. The SLM process involves a quick cooling to ambient temperature of around 10^6 K/s, which significantly reduces elements segregation [78]. Wang and his co-workers looked at how laser scan rates affected micro-segregation in selective laser melting. The inter-dendritic segregation ratio was shown to be lower as a result of their findings, which showed that higher scan rates caused larger cooling speeds [77]. Nb segregation is reduced as a result of enhanced cooling rates during QCW-LAM because there is not enough time for solute redistribution.

Second, the faster solidification speed produces better solute trapping, which prevents the proportion of Nb in the eutectic liquid from continuously rising and forming the Laves phase. More Nb atoms were trapped into the matrix in this case due to the quick solidification, leaving fewer Nb atoms and less opportunities for the development of the γ+ Laves eutectic microstructure. Due to this, using the QCW laser mode dramatically reduces the size, quantity, and Nb concentration of the Laves phase [79].

On the other hand, some scientists think that the faster solidification and dendritic development rates under QCW mode significantly enhance solute trapping and dendrite growth rates, leaving little time for Nb to permeate from the solid phase to the liquid phase. As a consequence, less Nb is left to form the Laves phase, and more Nb elements are trapped in the solid phase (matrix) [79]. Accelerated solidification causes solute atoms to be partitioned out of balance between the solid and the liquid. As a result, the solute separates out in the liquid that accumulates in the spaces between the already hardened dendrites, enriching the solidification process by two to five times the statutory component of the alloy element. Numerous elements present in the fluids cause complex elemental segregation in the inter-dendritic zones [80].

Some certain elements (Mo in 316L stainless steel, Nb in the In718, Si in AlSi10Mg, β stabilizing elements in Ti alloys, some elements in HEAs, etc.) undergo segregation during SLM process. It has been found that the anodic current density and passivity are significantly affected by the segregation of Mo. In order to create a passive layer, Mo is a necessary component. As a result, the passivation strategy may get worse due to its heterogeneous distribution in the alloy after SLM processing [81]. The elemental segregation of heavy metal ions—for example, Mo—at the boundaries may cause inhomogeneity of the microstructure [38].

The backscattered image of the SLM-processed alloy is depicted in Figure 10, which reveals a larger tendency for heavier elements, such as Mo (bright zones), to separate on the grain walls [59]. After five turns, there may be extreme refining and elemental segregation, which could affect the mechanical characteristics and corrosion resistance [82]. The accumulation of heavy elements on the grain walls of the SLM alloy [81] is shown by a backscattered electron micrograph of the alloy. Inside the cells are austenite stabilizing components, in contrast to the cell walls, which are higher in Mo, Cr, and Si. When ferrite stabilizer elements like Mo, Cr, and Si are displaced from the melt and trapped at the solid–melt contact point during rapid solidification in the SLM process, an austenitic microstructure is produced inside the cells. This enriches the cell walls with these elements [83].

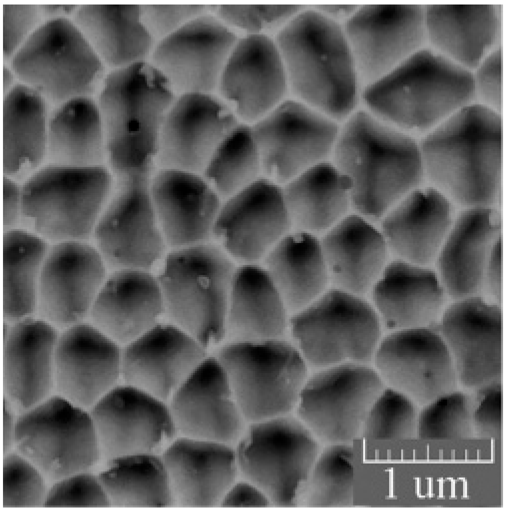

Figure 10. BSE micrograph of a SLM-produced 316L stainless steel, "Reprinted with permission from Ref. [59], 2021, Elsevier".

Some researchers have shown the segregation of elements in the cell walls of subgrains of metals. Figure 11 displays the line scan outcomes of the cell structure using Auger electron spectrometer (AES), indicating that Mo, Cr, and Ni elements segregate in the cell wall [84]. In other study, the intensity of the Mo Lα peak increased by more than 50%, indicating that Mo enrichment was seen near the cell borders. A boost of Mo in the intercellular areas was associated with a minor increase in the Ni Lα peak and a decrease in the C Kα peak. During the SLM process, elemental segregation may lead to the development of Mo-rich or carbide phases, which can deteriorate the corrosion characteristics [81]. Other researchers also reported the segregation of heavy metals at the cell walls [85,86].

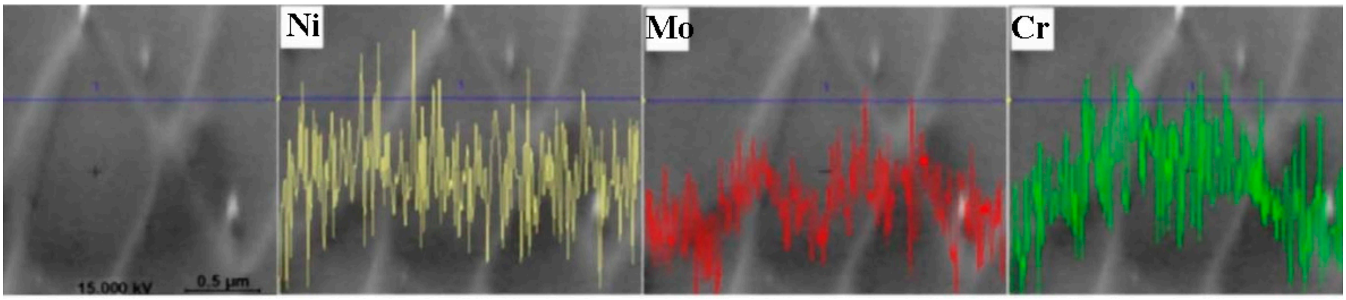

Figure 11. Elemental mapping of Ni (yellow line), Mo (red line), and Cr (green line) in the cell structure of 316L SS fabricated by SLM [84].

The Nb, Al, and Ti elements in the In718 samples were scanned using an EPMA map in Figure 12a–c. The creation of the Laves phases and the Nb-rich areas surrounding the Laves phases was made possible by the Nb element's predominate segregation in the inter-dendritic areas, as seen in Figure 12a of the as-fabricated specimen [87].

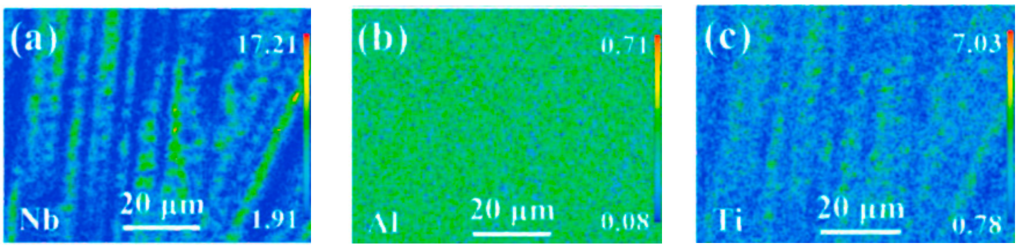

Figure 12. EPMA map scanning results of (**a**) Nb (**b**) Al, and (**c**) Ti, "Reprinted with Permission from Ref. [87], 2020, Elsevier."

SEM images of SLMed AlSi10Mg alloy samples in Figure 13a–c show the Si-rich cellular boundaries [88]. These cellular structures are formed as a result of the rapid solidification process that occurs during SLM, which leads to the formation of a cellular solidification front.

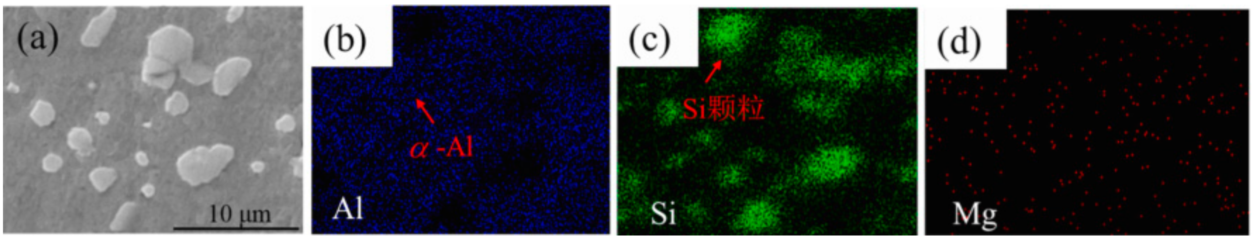

Figure 13. (**a**) microstructure of sample in building direction, (**b**) the element distribution of Al, (**c**) Si (Chinese content means Si particles), and (**d**) Mg, "Reprinted with Permission from Ref. [88], 2021, Elsevier".

In many cases, the SLM specimen showed lower segregations compared to the conventional counterparts. The findings of an EDS examination of Ni-Cr alloys are shown in Figure 14. The EDS maps of both SLM groups show a more homogeneous dispersion of the metal elements than those of the cast group, indicating superior corrosion resistance of the SLM alloys [89].

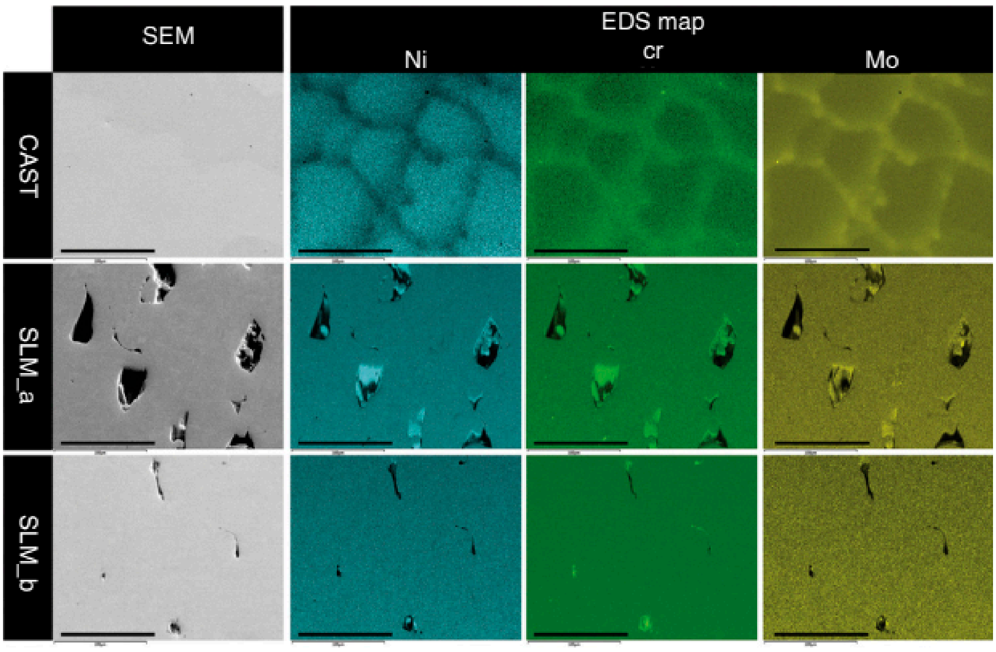

Figure 14. SEM and EDS analysis of cast and two SLM Ni-Cr alloy, "Reprinted with Permission from Ref. [89], 2019. Elsevier."

SLM-fabricated alloys frequently exhibit matrix super-saturation. Due to the quick solidification that occurs during SLM, some content cannot be separated out in this brief period and instead stays in solution in the matrix [24]. Some other researchers also showed that SLM-produced alloys can show a more uniform distribution of elements compared to conventionally produced alloys [5,60]. The uniform distribution of elements in SLM-produced alloys has significant implications for their properties and performances. It can lead to improvements in mechanical properties such as strength, ductility, and fatigue life, as well as corrosion resistance. Moreover, the ability to control the microstructures and compositions of SLM-produced alloys allows for the creation of customized materials with tailored properties for specific applications.

On the other hand, it is believed that there is a limitation in the characterization of segregation in the SLM parts. Some researchers reported that the segregation does not exist in the elements of alloys. At the same time, some other authors observed the elemental changes in a distinct period. This is likely due to the resolution limitation in the electron microscopies. For instance, as seen in Figure 15, an alloy that has undergone SLM processing does not clearly separate its components in the EDS images, especially Mo [6]. But, in the EDS-TEM image (Figure 16) acquired for the next stainless steel, it is possible to clearly see how Cr, Mo, Ni, and Mn segregate from the boundaries of the displacement cell [90]. It can be related to the higher spatial resolution in this work. Then, it can be concluded that the investigation of segregations for SLM alloys in most cases needs a high-resolution instrument to have a better judgment about the occurrence of segregation.

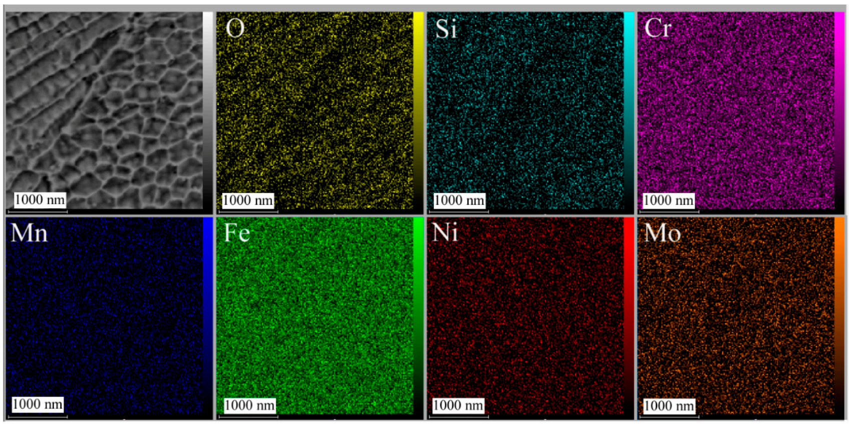

Figure 15. A cellular/dendritic SLM-treated 316L stainless steel with a FESEM images and EDS analysis. "Reprinted with Permission from Ref. [6], 2021, Elsevier".

Micro-segregation in the SLM alloys is one of those defects that may show dual effects. In some cases, it can act to strengthen mechanism sites, whereas, in some cases, it can act as an initiator for cracks. These situations will be discussed in the following. It has been reported by some authors that cracks are formed as a result of some specific elemental segregation that occurs at the grain boundaries [91–98]. For instance, it was claimed that the mechanical characteristics of metallic materials, such as strength, fatigue, toughness, etc., are significantly reduced by the segregation of Nb and the creation of the Laves phase [76,99]. High levels of alloying elements such as Mn, Si, S, and C can cause micro-segregation at grain boundaries during solidification, raising crack sensitivity, as Tomus and his coworkers noted [92]. The intergranular micro-cracks that were linked to Mo-rich carbide segregation were discovered to have developed consistently at the high-angle grain boundaries. Even though the interaction of the atoms Mo and Cr usually leads to the creation of carbides that also assist in controlling grain sizes and improve resilience to grain-boundary sliding, carbon does contribute to this process. This type of segregation increases the risk of hot splitting in nickel-based superalloys. This result demonstrates that structure segregation took place at the grain boundaries throughout the rapid solidification process [91].

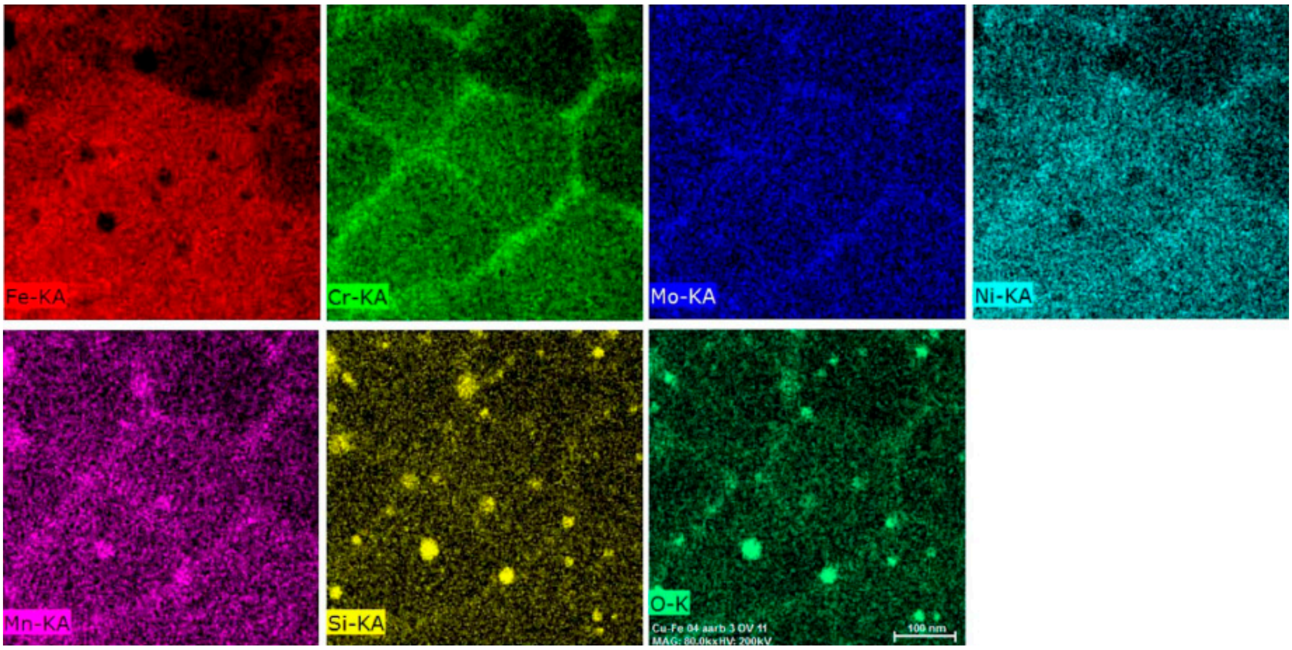

Figure 16. Chemical analyses of a 316l sample using an EDS-TEM [90].

The crack is clearly surrounded by C and Mo, whereas Ni and Fe are reduced nearby, as seen in Figure 17. There is no discernible concentration of these elements, in comparison to the observed Si and Mn segregation. The solidification cracking of Hastelloy X has been found to be significantly influenced by Si and C concentrations, although Tomus et al.'s investigation [21] has proven that the tendency for cracking was mostly independent of Mn level. Although in contrast to the findings of thermodynamic calculations by Tomus, EDS analysis of all cracks reveals a lack of Si segregation in this work, which is hypothesized due to the small Si content (0.087 wt.%) used in these trials [94].

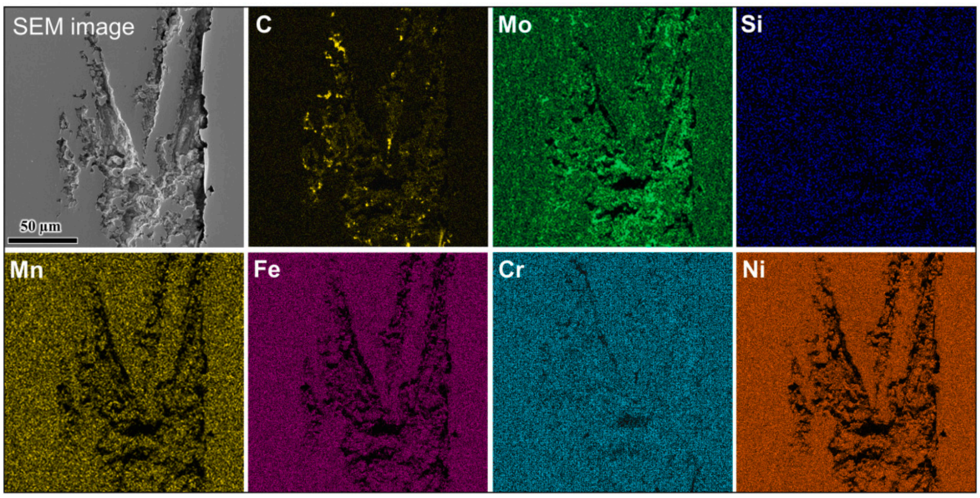

Figure 17. A crack's SEM micrograph and matching EDS analysis in the same region. "Reprinted with Permission from Ref. [94], 2022, Elsevier".

Also, some experts contend that the worse corrosion behavior of AM stainless steel may be caused by the micro-segregation of Mo in the cellular structure. It is possible that the chemical separation of heavy metals like Mo at the boundaries is what is causing the inhomogeneity of the morphology. When comparison to its wrought equivalent, the SLMed 316L stainless steel alloy showed reduced receptivity and a higher anodic current density in the HCl solution, according to Trelewicz and his colleagues [81]. The non-uniform arrangement of the components and the non-equilibrium morphologies created during the production process were blamed for the decreased resistance to corrosion [81]. Mo segregation has been found to have a considerable impact on the anodic current density and passivity decrease. For a passive layer to be established, Mo is a necessary component. Thus, the SLM alloy's uneven arrangement of it could impair the passivation process [6,81]. Oppositely, some researchers stated that the presence of segregation could enhance the mechanical performances of AM parts. According to Zhong et al. [85], the development of a distinctive intra-granular cellular segregation system morphology could help to boost yield strength without reducing ductility.

Recently, it was discovered that laser-processed pure 316L could form cellular structures, and this has validated the finding of segregation (such as Cr and Mo segregation) along the cellular pattern boundaries. Segregation engineering significantly aids in the strengthening of alloys [100,101]. Intragranular cellular borders that are more segregated serve as reinforcing elements within the grains. The intragranular micro- and nano-network, Mo-segregated encouragement, and oxide nano-inclusions all work together to improve the mechanical characteristics of SLM specimens through successfully reducing the rate of fracture development. This strengthening mechanism was confirmed by the high UTS values for SLM 316L SS samples that were collected during the tensile tests [85].

As other types of defects, there are some routes to reduce segregations in the SLM alloys. Using optimal parameters, changing the compositions, and using pulse lasers and some post treatments, including heat treatment, could reduce micro-segregation in the SLM alloys. Due to the quick cooling and solute entrapment, some studies found that greater scan speeds resulted in a lower inter-dendritic segregation ratio [77]. It was also reported that the addition of some ceramic particles could enhance the mechanical properties of an SLM part as well as reduce a few defects. For instance, Almangour and his colleagues reduced the sizes of the grains and melt pools by adding TiB_2 nanoparticles, indicating that the elements did not separate macroscopically. However, owing to the particle aggregation structure process, alloying components micro-segregated at the boundaries of cellular structures for greater TiB_2 levels [100]. Furthermore, it has been found that one of the best approaches to prevent cracks in the additive manufacture of HX is to reduce the level of carbon components to lessen the segregations of carbides in the additive process. The introduction of a nanoscale nucleation agent, which will promote heterogeneous nucleation and uniformed strains brought on by residual stress storage, is another approach that might be helpful [91].

Han et al. [102] reported that carbide segregation in the HX alloy was responsible for hot cracking. They proposed that the TiC nanoparticles, which changed the physical properties of the grain boundaries during the solidification process, were responsible for removing the hot fractures. The Marangoni force brought on by surface tension during the liquid–solid phase transition appears to have managed to separate the nanoparticle clusters rather than further agglomerate them, as evidenced by the relatively spherical morphologies of these particles and their independent occurrences in the matrix [102].

Some laser techniques have been reported that are suitable to reduce the segregation phenomenon in the SLM parts. Examples include the smaller heat-affected zone, lower dilution ratio, and more-refined grain refinement produced by pulsed laser additive manufacturing by a quasi-continuous wave (QCW) as opposed to the continuous wave counterpart [79,99,103]. The Nb segregation and Laves phase development of the Inconel 718 alloy were suppressed by a low average heat input and a high cooling speed from QCW [79]. The continuous wave (CW) and quasi-continuous wave (QCW) laser modes are shown schematically. Figure 18a,b, respectively, depict the LAM process. In QCW-LAM (Figure 18b), the laser power is regulated by a square wave with a duty cycle of 50% and a frequency of 10 Hz as opposed to CW-LAM, where the laser power is fixed at a given power [79].

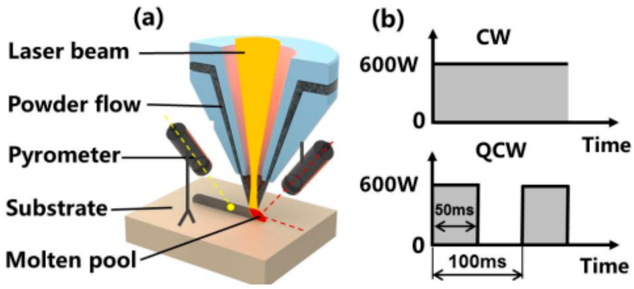

Figure 18. (**a**) a graphic illustration of the LAM method, as well as (**b**) Laser parameters for the CW and QCW patterns, "Reprinted with Permission from Ref. [79], 2017, Elsevier".

This dramatically enhances dendritic growth rate and solute entrapment with a higher cooling speed under QCW state, making it hard for Nb to permeate from the solid stage to the liquid stage inside an appropriate duration. This causes a greater proportion of Nb elements to be entrapped in the solid phase (matrix) and a lesser proportion to be left over to create the Laves phase. Hence, QCW mode efficiently lessens the system's impact of Nb segregation. [99]. Figure 19a,b shows the reduction in Laves phase and segregation after using pulse laser manufacturing.

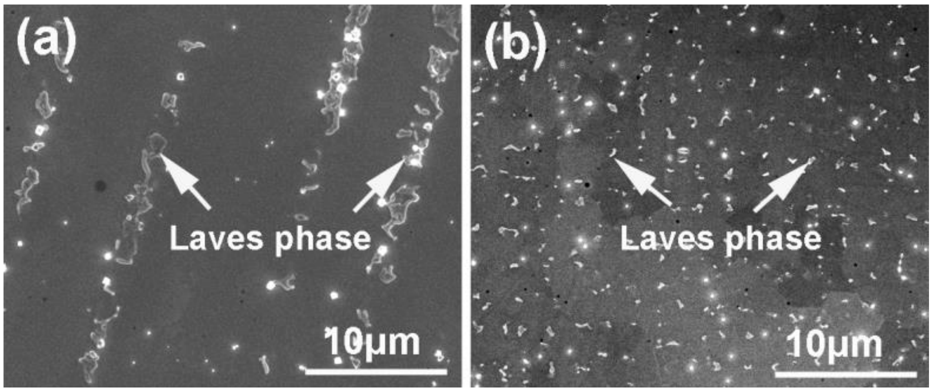

Figure 19. Laves phase shape usual of (**a**) CW specimen and (**b**) QCW specimen, "Reprinted with Permission from Ref. [79], 2017, Elsevier".

Another important strategy to reduce micro-segregation of SLM alloys is the application of heat treatment to obtain more uniform distribution of elements. Some researchers applied different heat treatment on the SLM alloys and observed the reduction in segregation after specific treatments [87,104,105]. On the In718 that had undergone SLM processing, Yu and his coworkers applied various thermal treatments in regard to: immediate aging (DA, 720 °C for 8 h, furnace cooling at 50 °C to 620 °C for 8 h), solution treatment plus aging (STA, 980 °C for 1 h, water cooling plus 720 °C for 8 h, furnace cooling at 50 °C to 620 °C for 8 h), and homogenization plus STA (HSTA, 1100 °C for 1.5 h, water cooling plus 980 °C for 1 h, water cooling plus 720 °C for 8 h) [87]. Nb, Al, and Ti components in the as-fabricated DA, STA, and HSTA specimens are shown in Figure 20a–l, which shows EPMA map scanning. The creation of the Laves phases and Nb-rich zones all over the Laves phases are facilitated by the Nb element's segregation in inter-dendritic regions of the as-fabricated specimen, as shown in Figure 20a. Nb segregation is still equal to the sample's as-fabricated state following DA post-heat treatment (Figure 20d), which might readily cause the deposition of γ'' phases in Nb-rich regions. The Nb segregation marginally diminishes during STA post-heat treatment (Figure 20g), which is caused by the lengthy migration of Nb atoms in high-temperature solution treatment conditions and the precipitate of the δ phase. Figure 20j illustrates how almost uniform the distribution of Nb in the matrix is following HSTA heat treatment. Al segregation is weaker than Nb segregation.

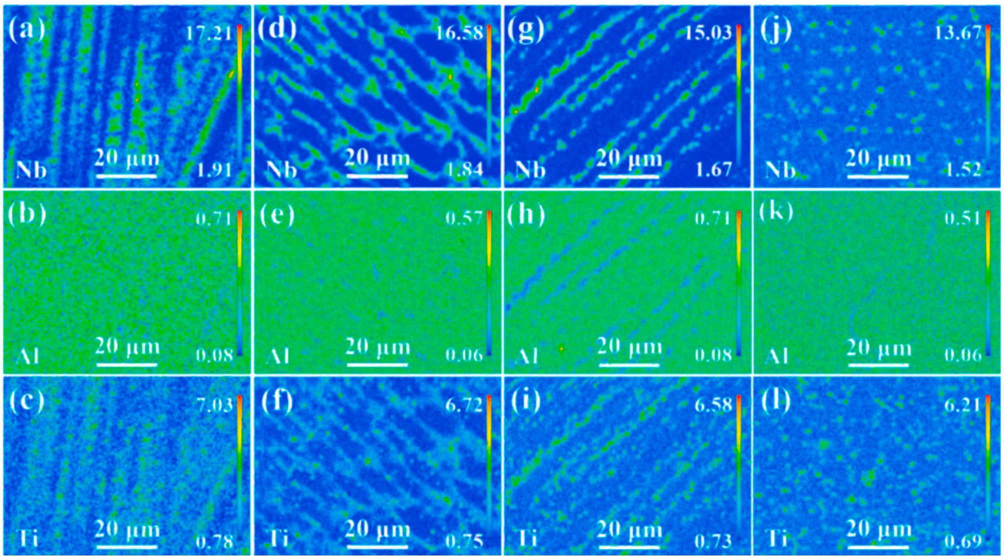

Figure 20. Nb, Al, and Ti map scan findings from EPMA: (**a**–**c**) As-fabricated, (**d**–**f**) DA, (**g**–**i**) STA, and (**j**–**l**) HSTA. "Reprinted with Permission from Ref. [87]. 2020. Elsevier".

However, Figure 20h shows that the Al element in the STA sample mainly segregates in the dendrite arms because it is a negative segregation element in the IN718 alloy. Although there is some variation in the segregation of Ti between all samples, this variation is not as significant as that of Nb. As a result, this partially explains how the heat treatment of the IN718 alloy affects the sizes and volume fractions of γ''/γ' precipitates. The as-fabricated and DA samples both exhibit a similar level of micro-segregation. The distribution of γ''/γ' precipitates in the dendritic arm becomes essentially uniform after STA, and micro-segregation declines. After HSTA, micro-segregation totally eliminates the γ''/γ' phases and causes them to deposit in large amounts (~30 nm) [87].

However, it should be noted that heat treatments do not necessarily reduce segregation. For instance, it was noted that heat treatment results in the deposition of stronger Mg_2Si intermetallic complexes as well as the segregation of Si from the aluminum phase [88,106]. Therefore, the application of post treatments needs to have enough knowledge about the response of elements in different phases.

6. Outlooks and Remarks

It seems that the pristine defects in the additive manufactured parts can be a disappointing issue to develop engineering shapes with desired characteristics. Some of these defects can also be present in the traditional counterparts such as cracks, LOF, keyholes, and segregations. But, some new defects in these parts arise from the fabrication methods, including melt pools, inclusions, and gas pores. Therefore, it is mandatory to overcome these new defects along with the reduction in classical ones. However, developing methods and techniques in the additive manufacturing industry can be a promising route to have hope in the future of financial complexes near net shapes with minimum defects. To achieve this, it is essential to invest in advanced techniques to create robust systems that are able to detect, mitigate, and eliminate defects during the manufacturing process.

7. Conclusions

Inclusions and segregations as defects of SLM metals were discussed in this review. It can be concluded that most defects can deteriorate on a special performance of AM alloys. But, some limited defects can lead to some better characteristics. For example, segregation and inclusion are not harmful in some cases and can enforce mechanical and chemical properties of alloys. On the other hand, some defects can trigger other defects. For example, some segregations can initiate cracks. In general, inclusions in an alloy can have a dual impact on performance. They can be useful if they hinder harmful phase formation and reduce the galvanic effect but can lead to deterioration if they have weak interfaces, agglomeration, or promote cracking and the galvanic effect. In the case of segregations, segregation in the micro-scale can be more harmful than in its nano-scale.

In total, it is better to avoid defects that can create discontinuities and heterogeneities in the SLM alloys. Special strategies should be performed to reduce such defects, including optimization the parameters, applying better quality of powders, changing the compositions, and post-processing treatments such as heat treatment. Moreover, it is crucial to understand the root cause of these defects to effectively prevent their occurrence. Monitoring and controlling the manufacturing process is critical to ensure that the material produced meets the required standards. By doing so, the quality and reliability of the final product can be significantly improved.

Author Contributions: Conceptualization, M.Y.; methodology, M.Y., Z.S.; Software, M.Y., Z.S., A.T.K., Z.H., F.S.; Validation, M.Y., Z.S.; Formal analysis, M.Y.; Investigation, M.Y.; Resources, M.Y., Z.S., A.T.K., Z.H., F.S.; Data curation, M.Y., Z.S., A.T.K., Z.H., F.S.; Writing—original draft, M.Y., Z.S., A.T.K., Z.H., F.S.; Writing—review and editing, M.Y., Z.S.; Visualization, M.Y., Z.S.; Supervision, M.Y.; Project administration, M.Y.; Funding acquisition, M.Y. All authors have read and agreed to the published version of the manuscript.

Funding: This research was funded by Shahid CHamran University of Ahvaz grant number [SCU. EM1401.31395].

Institutional Review Board Statement: Not applicable.

Informed Consent Statement: Not applicable.

Data Availability Statement: Not applicable.

Conflicts of Interest: The authors declare no conflict of interest.

References

1. Kumar, R.; Kumar, M.; Chohan, J.S. Material-specific properties and applications of additive manufacturing techniques: A comprehensive review. *Bull. Mater. Sci.* **2021**, *44*, 181. [CrossRef]
2. Blakey-Milner, B.; Gradl, P.; Snedden, G.; Brooks, M.; Pitot, J.; Lopez, E.; Leary, M.; Berto, F.; du Plessis, A. Metal additive manufacturing in aerospace: A review. *Mater. Des.* **2021**, *209*, 110008. [CrossRef]
3. Frazier, W.E. Metal additive manufacturing: A review. *J. Mater. Eng. Perform.* **2014**, *23*, 1917–1928. [CrossRef]
4. Jafferson, J.M.; Chatterjee, D. A review on polymeric materials in additive manufacturing. *Mater. Today Proc.* **2021**, *46*, 1349–1365. [CrossRef]
5. Yeganeh, M.; Shoushtari, M.T.; Jalali, P. Evaluation of the corrosion performance of selective laser melted 17-4 precipitation hardening stainless steel in Ringer's solution. *J. Laser Appl.* **2021**, *33*, 042001. [CrossRef]
6. Shaeri Karimi, M.H.; Yeganeh, M.; Alavi Zaree, S.R.; Eskandari, M. Corrosion behavior of 316L stainless steel manufactured by laser powder bed fusion (L-PBF) in an alkaline solution. *Opt. Laser Technol.* **2021**, *138*, 106918. [CrossRef]
7. Srivastava, M.; Rathee, S.; Patel, V.; Kumar, A. A review of various materials for additive manufacturing: Recent trends and processing issues. *J. Mater. Res. Technol.* **2022**, *21*, 2612–2641. [CrossRef]
8. Akessa, A.D.; Lemu, H.G. Overview study on challenges of additive manufacturing for a healthcare application. *IOP Conf. Ser. Mater. Sci. Eng.* **2021**, *1201*, 012041.
9. Bourell, D.; Kruth, J.P.; Leu, M.; Levy, G.; Rosen, D.; Beese, A.M.; Clare, A. Materials for additive manufacturing. *CIRP Ann.-Manuf. Technol.* **2017**, *66*, 659–681. [CrossRef]
10. Parandoush, P.; Lin, D. A review on additive manufacturing of polymer-fiber composites. *Compos. Struct.* **2017**, *182*, 36–53. [CrossRef]
11. Jahangir, N.; Arif, M.; Mamun, H.; Sealy, M.P. A review of additive manufacturing of magnesium alloys. *AIP Conf. Proc.* **2018**, *1980*, 030026. [CrossRef]
12. King, W.E.; Anderson, A.T.; Ferencz, R.M.; Hodge, N.E.; Kamath, C.; Khairallah, S.A.; Rubenchik, A.M. Laser powder bed fusion additive manufacturing of metals; physics, computational, and materials challenges. *Appl. Phys. Rev.* **2015**, *2*, 041304. [CrossRef]
13. Khairallah, S.A.; Anderson, A.T.; Rubenchik, A.; King, W.E. Laser powder-bed fusion additive manufacturing: Physics of complex melt flow and formation mechanisms of pores, spatter, and denudation zones. *Acta Mater.* **2016**, *108*, 36–45. [CrossRef]
14. Yap, C.Y.; Chua, C.K.; Dong, Z.L.; Liu, Z.H.; Zhang, D.Q.; Loh, L.E.; Sing, S.L. Review of selective laser melting: Materials and applications. *Appl. Phys. Rev.* **2015**, *2*, 041101. [CrossRef]

15. Wu, X.; Zhang, D.; Guo, Y.; Zhang, T.; Liu, Z. Microstructure and mechanical evolution behavior of LPBF (laser powder bed fusion)-fabricated TA15 alloy. *J. Alloys Compd.* **2021**, *873*, 159639. [CrossRef]
16. Huang, J.Y.; Chang, C.H.; Wang, W.C.; Chou, M.J.; Tseng, C.C.; Tu, P.W. Systematic evaluation of selective fusion additive manufacturing based on thermal energy source applied in processing of titanium alloy specimens for medical applications. *Int. J. Adv. Manuf. Technol.* **2020**, *109*, 2421–2429. [CrossRef]
17. Donik, C.; Kraner, J.; Paulin, I.; Godec, M. Influence of the Energy Density for Selective Laser Melting on the Microstructure and Mechanical Properties of Stainless Steel. *Metals* **2020**, *10*, 919. [CrossRef]
18. Zhang, B.; Li, Y.; Bai, Q. Defect Formation Mechanisms in Selective Laser Melting: A Review. *Chin. J. Mech. Eng.* **2017**, *30*, 515–527. [CrossRef]
19. Cruz, V.; Chao, Q.; Birbilis, N.; Fabijanic, D.; Hodgson, P.; Thomas, S. Electrochemical studies on the effect of residual stress on the corrosion of 316L manufactured by selective laser melting. *Corros. Sci.* **2020**, *164*, 108314. [CrossRef]
20. Chao, Q.; Cruz, V.; Thomas, S.; Birbilis, N.; Collins, P.; Taylor, A.; Hodgson, P.D.; Fabijanic, D. On the enhanced corrosion resistance of a selective laser melted austenitic stainless steel. *Scr. Mater.* **2017**, *141*, 94–98. [CrossRef]
21. Sander, G.; Babu, A.P.; Gao, X.; Jiang, D.; Birbilis, N. On the effect of build orientation and residual stress on the corrosion of 316L stainless steel prepared by selective laser melting. *Corros. Sci.* **2021**, *179*, 109149. [CrossRef]
22. Barroux, A.; Duguet, T.; Ducommun, N.; Nivet, E.; Delgado, J.; Laffont, L.; Blanc, C. Combined XPS/TEM study of the chemical composition and structure of the passive film formed on additive manufactured 17-4PH stainless steel. *Surf. Interfaces* **2021**, *22*, 100874. [CrossRef]
23. Barroux, A.; Ducommun, N.; Nivet, E.; Laffont, L.; Blanc, C. Pitting corrosion of 17-4PH stainless steel manufactured by laser beam melting. *Corros. Sci.* **2020**, *169*, 108594. [CrossRef]
24. Wei, W.; Zhou, Y.; Liu, W.; Li, N.; Yan, J.; Li, H. Microstructural Characterization, Mechanical Properties, and Corrosion Resistance of Dental Co-Cr-Mo-W Alloys Manufactured by Selective Laser Melting. *J. Mater. Eng. Perform.* **2018**, *27*, 5312–5320. [CrossRef]
25. Xie, F.; He, X.; Lv, Y.; Wu, M.; He, X.; Qu, X. Selective laser sintered porous Ti-(4-10)Mo alloys for biomedical applications: Structural characteristics, mechanical properties and corrosion behaviour. *Corros. Sci.* **2015**, *95*, 117–124. [CrossRef]
26. Čapek, J.; Machová, M.; Fousová, M.; Kubásek, J.; Vojtěch, D.; Fojt, J.; Jablonská, E.; Lipov, J.; Ruml, T. Highly porous, low elastic modulus 316L stainless steel scaffold prepared by selective laser melting. *Mater. Sci. Eng. C* **2016**, *69*, 631–639. [CrossRef]
27. Qi, T.; Zhu, H.; Zeng, X.; Yin, J. Effect of Si content on the cracking behavior of selective laser melted Al7050. *Rapid Prototyp. J.* **2019**, *25*, 1592–1600. [CrossRef]
28. Wang, D.; Yu, C.; Ma, J.; Liu, W.; Shen, Z. Densification and crack suppression in selective laser melting of pure molybdenum. *Mater. Des.* **2017**, *129*, 44–52. [CrossRef]
29. Li, H.; Ramezani, M.; Li, M.; Ma, C.; Wang, J. Tribological performance of selective laser melted 316L stainless steel. *Tribiol. Int.* **2018**, *128*, 121–129. [CrossRef]
30. Snow, Z.; Nassar, A.R.; Reutzel, E.W. Invited Review Article: Review of the formation and impact of flaws in powder bed fusion additive manufacturing. *Addit. Manuf.* **2020**, *36*, 101457. [CrossRef]
31. Vilanova, M.; Escribano-garcía, R.; Guraya, T.; Sebastian, M.S. Optimizing laser powder bed fusion parameters for IN-738LC by response surface method. *Materials* **2020**, *13*, 4879. [CrossRef] [PubMed]
32. Yadav, P.; Rigo, O.; Arvieu, C.; Le Guen, E.; Lacoste, E. In Situ Monitoring Systems of The SLM Process: On the Need to Develop Machine Learning Models for Data Processing. *Crystal* **2020**, *10*, 524. [CrossRef]
33. Huang, S.; Chen, B.; Liu, W.; Zhou, B.; Zhang, X.; Zeng, Q.; Guo, S. Effect of Heat Treatment on Microstructure and Properties of GH3536 Fabricated by Selective Laser Melting. *Metals* **2022**, *12*, 1184. [CrossRef]
34. Hong, M.; Min, B.K.; Kwon, T. The Influence of Process Parameters on the Surface Roughness of a 3D-Printed Co–Cr Dental Alloy Produced via Selective Laser Melting. *Appl. Sci.* **2016**, *6*, 401. [CrossRef]
35. Sabzi, H.E.; Rivera-díaz-del-castillo, P.E.J. Defect Prevention in Selective Laser Melting Components: Compositional and Process Effects. *Materials* **2019**, *12*, 3791. [CrossRef] [PubMed]
36. Trevisan, F.; Calignano, F.; Lorusso, M.; Pakkanen, J.; Aversa, A.; Ambrosio, E.P.; Lombardi, M.; Fino, P.; Manfredi, D. On the Selective Laser Melting (SLM) of the AlSi10Mg Alloy: Process, Microstructure, and Mechanical Properties. *Materials* **2017**, *10*, 76. [CrossRef]
37. Wu, L.; Zhao, Z.; Bai, P.; Zhang, Z.; Li, Y.; Liang, M.; Du, W. The Effect of Silicon Phase Morphology on Microstructure and Properties of AlSi10Mg Alloys Fabricated by Selective. *Materials* **2022**, *15*, 8786. [CrossRef]
38. Santamaria, R.; Salasi, M.; Rickard, W.D.A.; Pojtanabuntoeng, K.; Leadbeater, G.; Iannuzzi, M.; Reddy, S.M.; Quadir, Z. Crystallographic Texture and Substructural Phenomena in 316 Stainless Steel Printed by Selective Laser Melting. *Materials* **2023**, *16*, 4289. [CrossRef]
39. Saeidi, K.; Gao, X.; Zhong, Y.; Shen, Z.J. Hardened austenite steel with columnar sub-grain structure formed by laser melting. *Mater. Sci. Eng. A* **2015**, *625*, 221–229. [CrossRef]
40. Zhang, Z.; Yuan, X.; Zhao, Z.; Li, X.; Liu, B.; Bai, P. Electrochemical noise comparative study of pitting corrosion of 316L stainless steel fabricated by selective laser melting and wrought. *J. Electroanal. Chem.* **2021**, *894*, 115351. [CrossRef]
41. Moghadas, S.M.J.; Yeganeh, M.; Zaree, S.R.A.; Eskandari, M. Influence of low temperature heat treatment on microstructure, corrosion resistance and biological performance of 316L stainless steel manufactured by selective laser melting. *CIRP J. Manuf. Sci. Technol.* **2023**, *40*, 68–74. [CrossRef]

42. Sadeghi, E.; Karimi, P.; Israelsson, N.; Shipley, J.; Månsson, T.; Hansson, T. Inclusion-induced fatigue crack initiation in powder bed fusion of Alloy 718. *Addit. Manuf.* **2020**, *36*, 101670. [CrossRef]
43. Iams, A.D.; Keist, J.S.; Giannuzzi, L.A.; Palmer, T.A. The Evolution of Oxygen-Based Inclusions in an Additively Manufactured Super-Duplex Stainless Steel. *Metall. Mater. Trans. A* **2021**, *52*, 3401–3412. [CrossRef]
44. Kuah, K.X.; Salehi, M.; Ong, W.K.; Seet, H.L.; Ling, M.; Nai, S.; Wijesinghe, S.; Blackwood, D.J. Insights into the influence of oxide inclusions on corrosion performance of additive manufactured magnesium alloys. *npj Mater. Degrad.* **2022**, *6*, 36. [CrossRef]
45. Upadhyay, M.V.; Ben, M.; Slama, H.; Gaudez, S.; Mohanan, N.; Yedra, L.; Hallais, S.; Héripré, E.; Tanguy, A. Non-oxide precipitates in additively manufactured austenitic stainless steel. *Sci. Rep.* **2021**, *11*, 10393. [CrossRef] [PubMed]
46. Zheng, S.; Li, C.; Qi, Y.; Chen, L.; Chen, C. Mechanism of (Mg,Al,Ca)-oxide inclusion-induced pitting corrosion in 316L stainless steel exposed to sulphur environments containing chloride ion. *Corros. Sci.* **2013**, *67*, 20–31. [CrossRef]
47. Zhang, Y. Investigation of micro-electrochemical activities of oxide inclusions and microphases in duplex stainless steel and the implication on pitting corrosion. *Mater. Corros.* **2019**, *71*, 876–886. [CrossRef]
48. Hou, Y.; Zhao, J.; Cheng, C.; Zhang, L.; Li, J.; Liu, B.; Cao, T. The metastable pitting corrosion of 2205 duplex stainless steel under bending deformation. *J. Alloys Compd.* **2020**, *830*, 154422. [CrossRef]
49. Jeon, S.; Kim, H.; Park, Y. Effects of inclusions on the precipitation of chi phases and intergranular corrosion resistance of hyper duplex stainless steel. *Corros. Sci.* **2014**, *87*, 1–5. [CrossRef]
50. Liu, P.; Zhang, Q.; Watanabe, Y.; Shoji, T.; Cao, F. A critical review of the recent advances in inclusion-triggered localized corrosion in steel. *npj Mater. Degrad.* **2022**, *6*, 81. [CrossRef]
51. Vasconcellos da Costa e Silva, A.L. Non-metallic inclusions in steels–origin and control. *J. Mater. Res. Technol.* **2018**, *7*, 283–299. [CrossRef]
52. Saeidi, K.; Kvetková, L.; Lofaj, F.; Shen, Z. Austenitic stainless steel strengthened by the in situ formation of oxide nanoinclusions. *RSC Adv.* **2015**, *5*, 20747–20750. [CrossRef]
53. Andreatta, F.; Lanzutti, A.; Vaglio, E.; Totis, G.; Sortino, M.; Fedrizzi, L. Corrosion behaviour of 316L stainless steel manufactured by selective laser melting. *Mater. Corros.* **2019**, *70*, 1633–1645. [CrossRef]
54. Kong, D.; Dong, C.; Ni, X.; Zhang, L.; Yao, J.; Man, C.; Cheng, X.; Xiao, K.; Li, X. Mechanical properties and corrosion behavior of selective laser melted 316L stainless steel after different heat treatment processes. *J. Mater. Sci. Technol.* **2019**, *35*, 1499–1507. [CrossRef]
55. Ni, X.; Kong, D.; Wu, W.; Zhang, L.; Dong, C.; He, B.; Lu, L.; Wu, K.; Zhu, D. Corrosion Behavior of 316L Stainless Steel Fabricated by Selective Laser Melting Under Different Scanning Speeds. *J. Mater. Eng. Perform.* **2018**, *27*, 3667–3677. [CrossRef]
56. Ni, X.-Q.; Kong, D.-C.; Wen, Y.; Zhang, L.; Wu, W.-H.; He, B.-B.; Lu, L.; Zhu, D.-X. Anisotropy in mechanical properties and corrosion resistance of 316L stainless steel fabricated by selective laser melting. *Int. J. Miner. Metall. Mater.* **2019**, *26*, 319–328. [CrossRef]
57. Mohammadali, S.; Moghadas, J.; Yeganeh, M.; Reza, S.; Zaree, A.; Eskandari, M. The influence of heat treatment on the microstructure and corrosion behavior of selective laser melted 316L stainless steel in Ringer's solution. *Surf. Topogr. Metrol. Prop.* **2022**, *10*, 025012.
58. Soleimani, S.; Yeganeh, M.; Lari Baghal, S.M. Electrochemical behavior of laser powder bed fusion fabricated 316L stainless steel in a nitric acid solution. *J. Laser Appl.* **2022**, *34*, 042036. [CrossRef]
59. Yeganeh, M.; Rezvani, M.H.; Laribaghal, S.M. Electrochemical behavior of additively manufactured 316 L stainless steel in H_2SO_4 solution containing methionine as an amino acid. *Colloids Surf. A Physicochem. Eng. Asp.* **2021**, *627*, 127120. [CrossRef]
60. Shoushtari, M.T.; Yeganeh, M.; Kotoki, D.G. Enhanced corrosion resistance of 17-4 PH stainless steel fabricated by laser powder bed fusion in H_2SO_4 solution. *J. Laser Appl.* **2022**, *34*, 022023. [CrossRef]
61. Tiamiyu, A.A.; Eduok, U.; Szpunar, J.A.; Odeshi, A.G. Corrosion behavior of metastable AISI 321 austenitic stainless steel: Investigating the effect of grain size and prior plastic deformation on its degradation pattern in saline media. *Sci. Rep.* **2019**, *9*, 12116. [CrossRef]
62. Devendranath Ramkumar, K.; Pavan, B.; Chandrasekar, V. Development of improved microstructural traits and mechanical integrity of stabilized stainless steel joints of AISI 321. *J. Manuf. Process.* **2018**, *32*, 582–594. [CrossRef]
63. Lass, E.A.; Zhang, F.A.N.; Campbell, C.E. Nitrogen Effects in Additively Manufactured Martensitic Stainless Steels: Conventional Thermal Processing and Comparison with Wrought. *Metall. Mater. Trans. A* **2020**, *51*, 2318–2332. [CrossRef]
64. Hsu, T.; Chang, Y.; Huang, C.; Yen, H.; Chen, C.; Jen, K.; Yeh, A. Microstructure and property of a selective laser melting process induced oxide dispersion strengthened 17-4 PH stainless steel. *J. Alloys Compd.* **2019**, *803*, 30–41. [CrossRef]
65. Arya, C.; Vassie, P.R.W. Influence of cathode-to-anode area ratio and separation distance on galvanic corrosion currents of steel in concrete containing chlorides. *Cem. Concr. Res.* **1995**, *25*, 989–998. [CrossRef]
66. Dixit, S.; Liu, S. Laser Additive Manufacturing of High-Strength Aluminum Alloys: Challenges and Strategies. *J. Manuf. Mater. Process.* **2022**, *6*, 156. [CrossRef]
67. Iams, A.D.; Keist, J.S.; Palmer, T.A. Formation of Austenite in Additively Manufactured and Post-Processed Duplex Stainless Steel Alloys. *Metall. Mater. Trans. A* **2020**, *51*, 982–999. [CrossRef]
68. Zhang, M.; Xu, S.; Chu, Q.; Wang, B.; Zhang, L.; He, X.; Tong, X.; Zhang, L. Flux-Cored Wire for Arc Additive Manufacturing of Alloy Steel: Effect of Inclusion Particles on Microstructure and Properties. *J. Mater. Eng. Perform.* **2022**, *31*, 8955–8966. [CrossRef]

69. Irukuvarghula, S.; Hassanin, H.; Cayron, C.; Aristizabal, M.; Attallah, M.M. Acta Materialia Effect of powder characteristics and oxygen content on modi fications to the microstructural topology during hot isostatic pressing of an austenitic steel. *Acta Mater.* **2019**, *172*, 6–17. [CrossRef]
70. Lou, X.; Andresen, P.L.; Rebak, R.B. Oxide inclusions in laser additive manufactured stainless steel and their effects on impact toughness and stress corrosion cracking behavior. *J. Nucl. Mater.* **2018**, *499*, 182–190. [CrossRef]
71. Gong, H.; Dilip, J.J.S.; Yang, L.; Teng, C.; Stucker, B. Influence of small particles inclusion on selective laser melting of Ti-6Al-4V powder. *IOP Conf. Ser. Mater. Sci. Eng.* **2017**, *272*, 012024. [CrossRef]
72. Deng, P.; Karadge, M.; Rebak, R.B.; Gupta, V.K.; Prorok, B.C.; Lou, X. The origin and formation of oxygen inclusions in austenitic stainless steels manufactured by laser powder bed fusion. *Addit. Manuf.* **2020**, *35*, 101334. [CrossRef]
73. Kale, A.B.; Singh, J.; Kim, B.; Kim, D.; Choi, S. Effect of initial microstructure on the deformation heterogeneities of 316L stainless steels fabricated by selective laser melting processing. *Integr. Med. Res.* **2020**, *9*, 8867–8883. [CrossRef]
74. Moorehead, M.; Bertsch, K.; Niezgoda, M.; Parkin, C.; Elbakhshwan, M.; Sridharan, K.; Zhang, C.; Thoma, D.; Couet, A. High-throughput synthesis of Mo-Nb-Ta-W high-entropy alloys via additive manufacturing. *Mater. Des.* **2019**, *187*, 108358. [CrossRef]
75. Thapliyal, S.; Agrawal, P.; Agrawal, P.; Nene, S.S.; Mishra, R.S.; Mcwilliams, B.A.; Cho, K.C. Segregation engineering of grain boundaries of a metastable Fe-Mn-Co-Cr-Si high entropy alloy with laser-powder b e d fusion additive manufacturing. *Acta Mater.* **2021**, *219*, 117271. [CrossRef]
76. Xiao, W.; Xu, Y.; Xiao, H.; Li, S.; Song, L. Investigation of the Nb element segregation for laser additive manufacturing of nickel-based superalloys. *Int. J. Heat Mass Transf.* **2021**, *180*, 121800. [CrossRef]
77. Pontevedra, V.; Wang, Y.; Shi, J. Influence of laser scan speed on micro-segregation in selective laser melting of an iron-carbon alloy: A multi-scale simulation study. *Procedia Manuf.* **2018**, *26*, 941–951. [CrossRef]
78. Sun, Z.; Tan, X.; Tor, S.B.; Chua, C.K. Simultaneously enhanced strength and ductility for 3D-printed stainless steel 316L by selective laser melting. *NPG Asia Mater.* **2018**, *10*, 127–136. [CrossRef]
79. Xiao, H.; Li, S.; Han, X.; Mazumder, J.; Song, L. Laves phase control of Inconel 718 alloy using quasi-continuous-wave laser additive manufacturing. *Mater. Des.* **2017**, *122*, 330–339. [CrossRef]
80. Ghosh, S. Predictive modeling of solidification during laser additive manufacturing of nickel superalloys: Recent developments, future directions. *Mater. Res. Express* **2018**, *5*, 012001. [CrossRef]
81. Trelewicz, J.R.; Halada, G.P.; Donaldson, O.K.; Manogharan, G. Microstructure and Corrosion Resistance of Laser Additively Manufactured 316L Stainless Steel. *JOM* **2016**, *68*, 850–859. [CrossRef]
82. Mohd Yusuf, S.; Nie, M.; Chen, Y.; Yang, S.; Gao, N. Microstructure and corrosion performance of 316L stainless steel fabricated by Selective Laser Melting and processed through high-pressure torsion. *J. Alloys Compd.* **2018**, *763*, 360–375. [CrossRef]
83. Prashanth, K.G.; Eckert, J. Formation of metastable cellular microstructures in selective laser melted alloys. *J. Alloys Compd.* **2017**, *707*, 27–34. [CrossRef]
84. Yang, D.; Yin, Y.; Kan, X.; Zhao, Y.; Zhao, Z. The mechanism of substructure formation and grain growth 316L stainless steel by selective laser melting. *Mater. Res. Express* **2021**, *8*, 096510. [CrossRef]
85. Zhong, Y.; Liu, L.; Wikman, S.; Cui, D.; Shen, Z. Intragranular cellular segregation network structure strengthening 316L stainless steel prepared by selective laser melting. *J. Nucl. Mater.* **2016**, *470*, 170–178. [CrossRef]
86. Ziętala, M.; Durejko, T.; Polański, M.; Kunce, I.; Płociński, T.; Zieliński, W.; Łazińska, M.; Stępniowski, W.; Czujko, T.; Kurzydłowski, K.J.; et al. The microstructure, mechanical properties and corrosion resistance of 316L stainless steel fabricated using laser engineered net shaping. *Mater. Sci. Eng. A* **2016**, *677*, 1–10. [CrossRef]
87. Yu, X.; Lin, X.; Liu, F.; Wang, L.; Tang, Y.; Li, J.; Zhang, S.; Huang, W. Influence of post-heat-treatment on the microstructure and fracture toughness properties of Inconel 718 fabricated with laser directed energy deposition additive manufacturing. *Mater. Sci. Eng. A* **2020**, *798*, 140092. [CrossRef]
88. Wei, P.; Chen, Z.; Zhang, S.; Fang, X.; Lu, B.; Zhang, L.; Wei, Z. Effect of T6 heat treatment on the surface tribological and corrosion properties of AlSi10Mg samples produced by selective laser melting. *Mater. Charact.* **2021**, *171*, 110769. [CrossRef]
89. Hong, M.; Hanawa, T.; Hoon, S.; Ki, B.; Kwon, T. Enhanced biocompatibility of a Ni–Cr alloy prepared by selective laser melting: A preliminary in vitro study. *J. Mater. Res. Technol.* **2019**, *8*, 1587–1592. [CrossRef]
90. Gorsse, S.; Hutchinson, C.; Gouné, M.; Banerjee, R. Additive manufacturing of metals: A brief review of the characteristic microstructures and properties of steels, Ti-6Al-4V and high-entropy alloys. *Sci. Technol. Adv. Mater.* **2017**, *18*, 584–610. [CrossRef]
91. Han, Q.; Gu, Y.; Soe, S.; Lacan, F.; Setchi, R. Effect of hot cracking on the mechanical properties of Hastelloy X superalloy fabricated by laser powder bed fusion additive manufacturing. *Opt. Laser Technol.* **2020**, *124*, 105984. [CrossRef]
92. Tomus, D.; Jarvis, T.; Wu, X.; Mei, J.; Rometsch, P.; Herny, E.; Rideau, J.-F.; Vaillant, S. Controlling the microstructure of Hastelloy-X components manufactured by selective laser melting. *Phys. Procedia* **2013**, *41*, 823–827. [CrossRef]
93. Marchese, G.; Basile, G.; Bassini, E.; Aversa, A.; Lombardi, M.; Ugues, D.; Fino, P.; Biamino, S. Study of the Microstructure and Cracking Mechanisms of Hastelloy X Produced by Laser Powder Bed Fusion. *Materials* **2018**, *11*, 106. [CrossRef]
94. Guo, B.; Zhang, Y.; Yang, Z.; Cui, D.; He, F.; Li, J.; Wang, Z.; Lin, X.; Wang, J. Cracking mechanism of Hastelloy X superalloy during directed energy deposition additive manufacturing. *Addit. Manuf.* **2022**, *55*, 102792. [CrossRef]
95. Xu, Z.; Jiang, L.; Dong, J.; Li, Z.; Zhou, X. The effect of silicon on precipitation and decomposition behaviors of M6C carbide in a Ni–Mo–Cr superalloy. *J. Alloys Compd.* **2015**, *620*, 197–203. [CrossRef]

96. Tomus, D.; Rometsch, P.A.; Heilmaier, M.; Wu, X. Effect of minor alloying elements on crack-formation characteristics of Hastelloy-X manufactured by selective laser melting. *Addit. Manuf.* **2017**, *16*, 65–72. [CrossRef]
97. Wang, G.; Huang, L.; Tan, L.; Qin, Z.; Chen, C.; Liu, F.; Zhang, Y. Effect of yttrium addition on microstructural evolution and high temperature mechanical properties of Ni-based superalloy produced by selective laser melting. *Mater. Sci. Eng. A* **2022**, *859*, 144188. [CrossRef]
98. Kumar, M.; Gibbons, G.J.; Das, A.; Manna, I.; Tanner, D.; Kotadia, H.R. Additive manufacturing of aluminium alloy 2024 by laser powder bed fusion: Microstructural evolution, defects and mechanical properties. *Rapid Prototyp. J.* **2021**, *7*, 1388–1397. [CrossRef]
99. Xiao, H.; Li, S.M.; Xiao, W.J.; Li, Y.Q.; Cha, L.M.; Mazumder, J.; Song, L.J. Effects of laser modes on Nb segregation and Laves phase formation during laser additive manufacturing of nickel-based superalloy. *Mater. Lett.* **2016**, *188*, 260–262. [CrossRef]
100. Almangour, B.; Kim, Y.; Grzesiak, D.; Lee, K. Novel TiB_2-reinforced 316L stainless steel nanocomposites with excellent room- and high-temperature yield strength developed by additive manufacturing. *Compos. Part B* **2018**, *156*, 51–63. [CrossRef]
101. Abramova, M.M.; Enikeev, N.A.; Valiev, R.Z.; Etienne, A.; Radiguet, B.; Ivanisenko, Y.; Sauvage, X. Grain boundary segregation induced strengthening of an ultrafine-grained austenitic stainless steel. *Mater. Lett.* **2014**, *136*, 349–352. [CrossRef]
102. Han, Q.; Gu, Y.; Setchi, R.; Lacan, F.; Johnston, R.; Evans, S.L.; Yang, S. Additive manufacturing of high-strength crack-free Ni-based Hastelloy X superalloy. *Addit. Manuf.* **2019**, *30*, 100919. [CrossRef]
103. Ravi, G.A.; Qiu, C.; Attallah, M.M. Microstructural control in a Ti-based alloy by changing laser processing mode and power during direct laser deposition. *Mater. Lett.* **2016**, *179*, 104–108. [CrossRef]
104. Lopez-galilea, I.; Ruttert, B.; He, J.; Hammerschmidt, T.; Drautz, R.; Gault, B.; Theisen, W. Additive manufacturing of CMSX-4 Ni-base superalloy by selective laser melting: Influence of processing parameters and heat treatment. *Addit. Manuf.* **2019**, *30*, 100874. [CrossRef]
105. Raghavan, S.; Zhang, B.; Wang, P.; Sun, C.-N.; Nai, M.L.S.; Li, T.; Wei, J. Effect of different heat treatments on the microstructure and mechanical properties in selective laser melted INCONEL 718 alloy. *Mater. Manuf. Process.* **2016**, *32*, 1588–1595. [CrossRef]
106. Girelli, L.; Giovagnoli, M.; Tocci, M.; Pola, A.; Fortini, A.; Merlin, M.; Marina, G.; Vecchia, L. Evaluation of the impact behaviour of AlSi10Mg alloy produced using laser additive manufacturing. *Mater. Sci. Eng. A* **2019**, *748*, 38–51. [CrossRef]